The Astrophysical Journal, 919:104 (17pp), 2021 October 1 https://doi.org/10.3847/1538-4357/ac1069

Radiative Transfer Modeling of an SN 1987A Light Echo—AT 2019xis

Jiachen Ding[1], Lifan Wang[2], Peter Brown[2], and Ping Yang[1]
[1] Department of Atmospheric Sciences, Texas A&M University, College Station, TX 77843, USA; njudjc@tamu.edu
[2] Department of Physics and Astronomy, Texas A&M University, College Station, TX 77843, USA
Received 2021 April 8; revised 2021 June 29; accepted 2021 June 29; published 2021 September 29

Abstract

We use a Monte Carlo radiative transfer model (MCRTM) to simulate the *UBVRI* light curves, images, and linear polarization of a light echo from supernova SN 1987A in the Large Magellanic Cloud (LMC) using various dust cloud shapes, sizes, and optical properties. We compare the theoretical simulations to the observations of AT 2019xis, a light echo detected at a large angular distance (4.′05) from SN 1987A. We estimate the size and optical thickness of the dust cloud based on the simulation results and the observations of the Optical Gravitational Lensing Experiment (OGLE-IV) Transient Detection System (OTDS) *I*-band light curve. The mass of the dust cloud is calculated using the estimated size, optical thickness, and extinction coefficient. If the dust cloud is assumed to correspond to a gas-to-dust ratio of 300, the total mass of the dust cloud is approximately 7.8–9.3 $M_{\odot}$. Based on these theoretical models, we show that the morphological shapes of the light echoes in the wavelength range of or shorter than the *U* band to be very different from those in the longer wavelength bands, and the difference carries important information on the early UV radiation of SN 1987A.

Unified Astronomy Thesaurus concepts: Interstellar dust (836); Interstellar scattering (854); Interstellar clouds (834); Core-collapse supernovae (304); Radiative transfer simulations (1967); Type II supernovae (1731)

1. Introduction

A light echo (LE) is the scattered starlight by an interstellar or circumstellar dust cloud. The scattered photons of an LE travel along different paths from the direct line of sight, so an LE is always observed at a time after the source light arrives at the observer. Sometimes more than one LE is observed at the same time. In this case, the scattered photons of each LE propagate the same distance from the source to the observer but do not travel via the same path.

The LE generation mechanism and geometry can be described by an ellipsoid model if only single scattering is considered. The light source and observer are at two foci of a prolate spheroid. The distance from the light source to any point on the spheroidal surface plus the distance from the point to the observer is a constant, which corresponds to a single delay time. In practical astronomical observation, the observer can be assumed to be infinitely far from the LE source. The ellipsoid model can thus be simplified to a paraboloid model (Couderc 1939). Figure 1 illustrates the paraboloid model in 2D, which is a parabola in the *yz* plane. The intersection of any paraboloid with the *xy* plane, corresponding to a telescope field of view, is a circle centered on the *z*-axis at the source coordinate.

For any parabola in Figure 1, the delay time is t_d, the distance from the light source to a scattering dust cloud is l, the distance between the scattering dust cloud and the light source's line of sight is ρ, and the dust cloud scattering angle is θ. Based on the parabola model, we have the following relations for any scattering object:

$$l = \frac{1}{2}\left(\frac{\rho^2}{ct_d} + ct_d\right), \tag{1a}$$

$$\cos\theta = \frac{\rho^2 - (ct_d)^2}{\rho^2 + (ct_d)^2}, \tag{1b}$$

where c is the speed of light. l and θ can be estimated based on Equation 1(a) if ρ and t_d are known. ρ and t_d can be accurately measured in LE observations, provided that the light source is identified. More detailed descriptions of the LE paraboloid model have been reported in previous studies (e.g., Chevalier 1986; Sparks 1994; Sugerman 2003; Tylenda 2004; Patat 2005). Single scattering usually dominates the observed LE signal so the paraboloid model is still useful to analyze LE observations with some multiple scattering contribution. In Figure 1, the three parabolas correspond to three delay times. Although Paths 1 and 2 are different, the scattering points S_1 and S_2 are on the same parabola, and the path lengths to the observer are the same, so the scattered light traveling via these paths can be observed at the same time.

While any star can produce an LE, a substantial amount of information can be obtained if the source light comes from transients such as supernovae (SNe) and novae, or other variable objects such as Miras and Cepheids (Sugerman 2003). An LE contains information such as spectra of the source light that illuminated the dust cloud, so LEs can be used to trace the characteristics of historical SNe (e.g., Rest et al. 2005; Dwek & Arendt 2008; Rest et al. 2008, 2012a), which have exploded many years ago. On the other hand, an LE also carries fruitful information about the dust cloud (Rest et al. 2012b) including optical properties, grain size, and composition.

Understanding the properties of interstellar dust is important from various aspects of astronomical research. This is because astronomical observations are usually affected by interstellar dust extinction along the path to Earth. To obtain the absolute brightness of a star such as an SN, we need to correct for extinction by interstellar dust. For example, Type Ia SNe can be used as extragalactic distance indicators (e.g., Riess et al. 1996; Perlmutter et al. 1998) in cosmology studies. The uncertainties in distance estimation using Type Ia SNe can be reduced if dust extinction is accurately accounted for. Interstellar dust also plays a critical role in star formation and galaxy evolution.

Interstellar dust extinction can be directly measured along the line of sight (e.g., Clayton & Martin 1985; Fitzpatrick 1986;

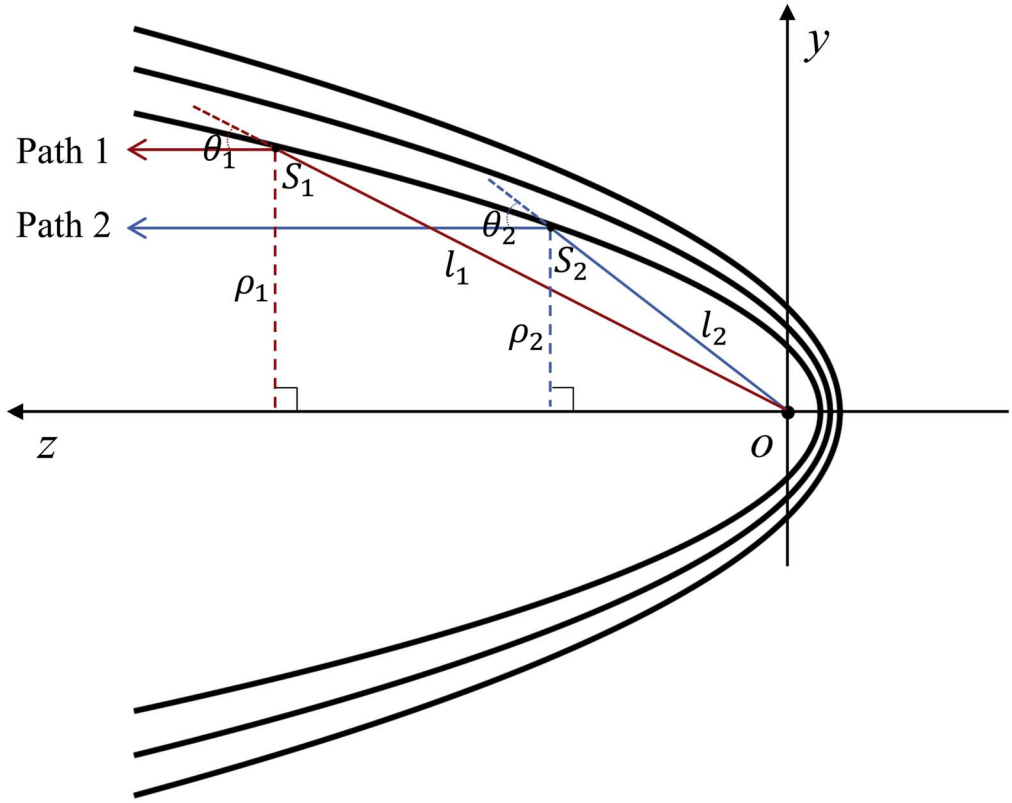

Figure 1. Parabola illustration of light echo geometry in 2D. The light source is at origin O. The light source–observer line of sight is along the z-direction, and the delay time is zero at any point on the z-axis. The three parabolas correspond to three nonzero delay times, with the inner parabola having a smaller delay. Two scattering points (S_j, $j = 1, 2$) and their light travel paths are plotted on the inner parabola. For scattering point S_j, l_j is the distance from O to S_j, ρ_j is the orthogonal distance from S_j to the light source's line of sight on the z-axis, and θ_j is the scattering angle along that light travel path. Each point on a parabola has the same delay time.

Cardelli et al. 1988). In observations along the line of sight, the scattered light cannot be fully separated from the directly transmitted light and the dust property information is only limited to a single sight line. In contrast, LEs may contain scattered light alone along various photon travel paths. The two-dimensional image and even three-dimensional structure of a dust cloud can be inferred by LE observations. Previous studies (e.g., Nova Persei 1901 LEs by Couderc 1939; SN 1987A LEs by Crotts 1988; Suntzeff et al. 1988; Xu et al. 1995; SN 2006X LEs by Wang et al. 2008; SN 2007af LEs by Drozdov et al. 2015; SN 2014J LEs by Crotts 2015; Yang et al. 2017 to list just a few) successfully utilize LEs to infer interstellar and circumstellar dust properties.

Considering interstellar dust concentration and optical properties, the brightness of an LE is approximately 10 mag fainter than the source light that illuminates the dust cloud (Patat 2005). Because SNe can be highly luminous at their peak brightness and their explosion is like a flash, the LEs induced by SNe are easier to observe and are used to study interstellar/circumstellar dust properties. The Type II SN 1987A (Arnett et al. 1989; McCray & Fransson 2016) in the Large Magellanic Cloud (LMC) is the SN closest to Earth that people have observed since Kepler's Supernova. Many SN 1987A LEs have been captured and utilized to infer the characteristics of SN 1987A and its nearby dust.

LEs scattered by interstellar dust about 100–400 pc in front of SN 1987A are first observed and identified using imaging and spectroscopy (Crotts 1988; Gouiffes et al. 1988; Suntzeff et al. 1988; Couch et al. 1990) as predicted by Schaefer (1987) and Chevalier & Emmering (1988). At distances of several arcseconds to SN 1987A, Crotts et al. (1989) discovered diffuse radiations that are well resolved to be nebular rings by images taken at the ESO NTT (Wampler et al. 1990; Wang & Wampler 1992). Wampler et al. (1990) show also evolving diffuse light immediately outside the nebular rings, which is known as Napoleon's Hat nebula (Wang & Wampler 1992). While the rings are modeled in terms of the interaction between the low-velocity wind presumably from the progenitor during the red supergiant (RSG) phase with a subsequent energetic fast wind during the blue supergiant (BSG) phase (Wang & Mazzali 1992), Napoleon's Hat nebula is found to be produced by dusty materials lost during the RSG, and the bow-shock-like morphology is caused by a differential motion between the progenitor star and the interstellar matter (Wang & Wampler 1992; Wang et al. 1993). Xu et al. (1995) mapped the 3D interstellar dust structure in front of SN 1987A using more than 5 yr of LE images. With the decrease of SN 1987A brightness, more LEs scattered by circumstellar dust were also observed and resolved (Crotts et al. 1989; Bond et al. 1990; Wampler et al. 1990; Wang & Wampler 1992). SN 1987A LE images are used to probe the three-ring circumstellar dust structure around SN 1987A (e.g., Wang et al. 1993; Sugerman et al. 2005a, 2005b). Model calculations suggest that circumstellar dust scattering or LE may significantly contribute to the observed SN 1987A polarization (Wang & Wheeler 1996).

A recently observed transient, AT 2019xis in the LMC has been identified as an LE of SN 1987A (Taubenberger et al. 2019) through the I-band light curve and spectrum comparisons. The angular distance between SN 1987A and AT 2019xis is about

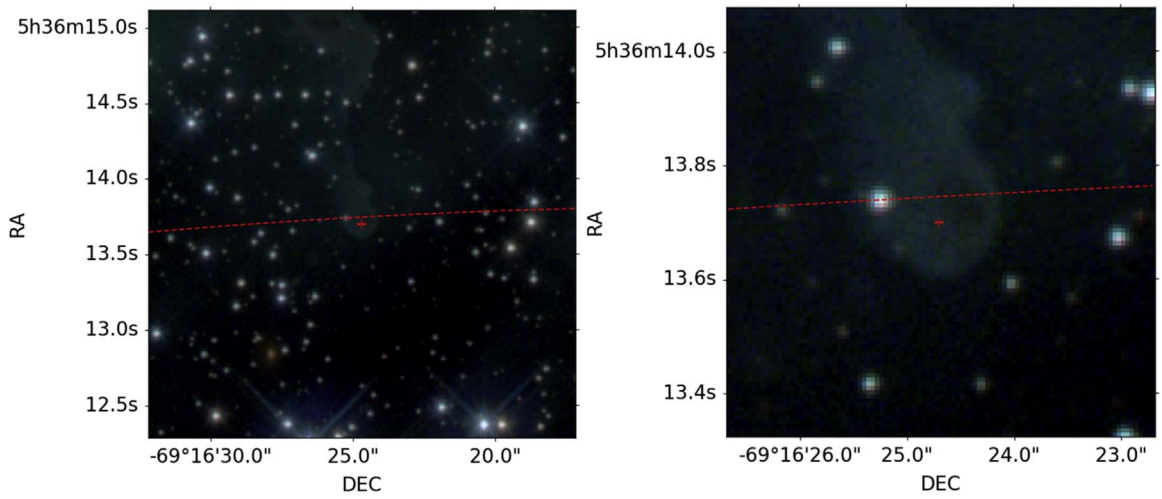

Figure 2. RGB images from 2014 showing the region where AT 2019xis was observed. The RGB images are plotted using HST WFC3 data. Astronomical north (increasing decl.) is at the right of each image and astronomical east (increasing R.A.) is at the top. The red cross denotes the coordinate of AT 2019xis (R.A. 05:36:13.700, decl. −69:16:24.70). The red dashed line across the middle of each panel is the intersection between the field of view and the SN 1987A light echo paraboloid at the distance and decl. of AT 2019xis. Left image: measures 15″ × 15″; Right image: measures 4″ × 4″.

4.′05 and the geometric distance is about 200 pc or ≈650 lt-yr (Taubenberger et al. 2019). Represented schematically by Path 1 in Figure 1, l_1 is the distance from SN 1987A to AT 2019xis, and the Path 1 and y-axis arrows intersect at Earth at a 4.′05 angle. This angular distance is far larger than previously observed in Napoleon's Hat (Wang & Wampler 1992; Wang et al. 1993), so the impact of a directly transmitted source light can be completely excluded and the dust scattering angle is large (≈20°; angle θ_1 in Figure 1). Because the scattering angle is large, the strong forward scattering by the dust cloud hardly contributes to the LE signal, and the LE brightness must be far weaker than the source light. Thus, the SN needs to be very nearby to make such an LE observable. AT 2019xis is a unique LE to study interstellar dust optical properties at a large scattering angle.

Figure 2 shows RGB images from 2014 August where AT 2019xis was observed in 2019. The images are composed of archival Hubble Space Telescope (HST) Wide Field Camera 3 (WFC3) UVIS channel observations (# 13401, PI: Claes Fransson) obtained from the Mikulski Archive for Space Telescopes (MAST; no comparable images showing the AT 2019xis LE are available). There is a detailed list of images in Table A1, in Appendix A. The red (R), green (G), and blue (B) channels use HST data from the F814W, F606W, and F475W filters, respectively. The medians of the pixel values in images of an individual filter are used to construct the image in a color channel. Because at the time the HST images were taken, the SN 1987A emission has not yet arrived at the AT 2019xis location, the signal in Figure 2 is emission by the dust cloud. Around the location of AT 2019xis, the dust cloud has a disk-like shape with a nonconcentric hole. The left plot of Figure 2 shows that the disk-like structure is part of a larger dust cloud. The LE was from a reflective patch with dimension ≈0.6 lt-yr (Figure 2; Taubenberger et al. 2019), or about half of the width of the visible dust cloud around AT 2019xis, so other LEs may be observed in the future from the remaining part of the dust cloud.

The AT 2019xis dust cloud has a similar distance to the SN 1987A along the line of sight (about 170 pc) as the previously discovered circular echoes (e.g., Crotts 1988; Gouiffes et al. 1988; Suntzeff et al. 1988; Couch et al. 1990). However, the AT 2019xis dust cloud has a much larger angular distance (approximately 4.′05) from the SN. If we assume an LE by a dust cloud that is at the same distance along the line of sight to the SN 1987A as the AT 2019xis dust cloud is observed one year after the SN 1987A explosion, the distance between the AT 2019xis dust cloud and the assumed dust cloud is about 50 pc. Therefore, the AT 2019xis dust cloud may be part of a superbubble that is in front of SN 1987A.

Models of the LE brightness and time evolution are always needed to infer meaningful information from the LE observations. The single-scattering approximation can be used in modeling LEs (e.g., Chevalier 1986; Schaefer 1987; Wang & Wheeler 1996; Sugerman 2003; Patat 2005) if the dust cloud is optically thin. Under the single-scattering approximation, the LE brightness is expressed as a product of source light flux, dust scattering phase function and scattering efficiency, and dust concentration. The ellipsoid or paraboloid model is used to analyze LE time evolution. If the dust cloud is optically thick and dense such as the dust cloud of AT 2019xis, multiple scattering contributions must be included. Monte Carlo techniques have been used to simulate the radiative transfer process of LEs (e.g., Witt 1977; Chevalier 1986; Patat 2005; Wang 2005; Patat et al. 2006), which can take into account multiple scattering effects.

In this study, we use a Monte Carlo radiative transfer model (MCRTM) to simulate the observation of an interstellar dust cloud with similar observing geometry to AT 2019xis and show how the simulated observations vary with different dust optical properties, dust cloud sizes, and shapes. We also estimate the dust cloud properties using our simulation results and I-band light-curve observations from the Optical Gravitational Lensing Experiment (OGLE-IV) Transient Detection System (OTDS; Kozłowski et al. 2013; Wyrzykowski et al. 2014). In the following sections, we introduce the methodology and observations in Section 2, present the simulation and estimation results in Section 3, and summarize the study in Section 4.

2. Methodology

2.1. Radiative Transfer Simulation

The MCRTM is used to simulate the observation of the SN 1987A LE by the dust cloud at AT 2019xis location and

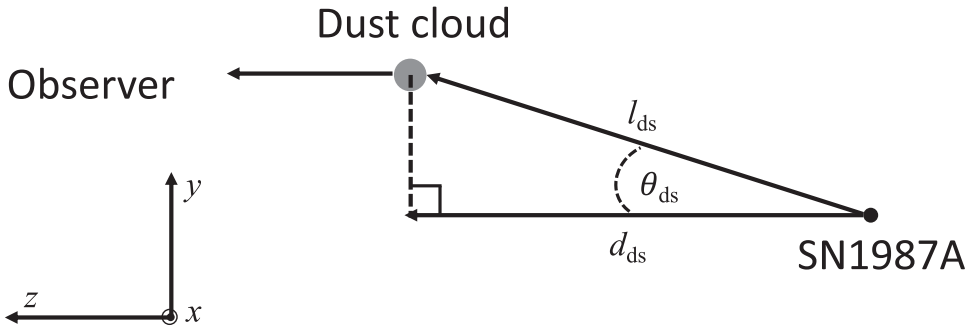

Figure 3. Modeled observational geometry. SN 1987A is at the origin. l_{ds} is the distance between the dust cloud center and SN 1987A. d_{ds} is the distance between the dust cloud and SN 1987A along the line of sight or z-direction. θ_{ds} is the viewing angle looking from SN 1987A to the dust cloud and is also the single-scattering angle.

outputs the LEs Stokes vector. A detailed description of the MCRTM is in Appendix B.

The modeled observational geometry is illustrated in Figure 3. The dust cloud and SN 1987A are in the yz plane. The polarization reference plane of the observed Stokes vector is the xz plane. The xy plane is divided into a variety of square bins to simulate the LE image. At each scattering position, if the x and y coordinates are within a predefined square bin, the contribution of the photon is counted to the LE at the center of this square bin.

2.2. Interstellar Dust Optical Properties

In the radiative transfer simulation involving a dust cloud, the interstellar dust optical properties including extinction cross section (C_{ext}), SSA, and scattering phase matrix are needed. In this study, we adopt the optical properties of the dust grain model developed by Weingartner & Draine (2001), Li & Draine (2001), and Draine & Li (2007) (hereafter the WD01 model).

The WD01 dust grain model assumes the dust grain is a mixture of carbonaceous and silicate particles and has a grain-size distribution with more than 10 adjustable parameters. The grain size ranges from 3.5 Å–10 μm. The dust particle shape is assumed to be a sphere. Mie theory is utilized to obtain the single-scattering properties of the dust particle (Weingartner & Draine 2001). The dust grain model can reproduce observed interstellar dust extinction and emission (Li & Draine 2001; Weingartner & Draine 2001) by adjusting the grain-size distribution parameters. In this study, we consider dust models in the LMC, Small Magellanic Cloud (SMC), and Milky Way (MW) including six models, namely "LMC avg," "LMC 2," "SMC bar," and three MW dust models with different total-to-selective extinction ratios (R_V).

Each dust grain model in Weingartner & Draine (2001) has multiple sets of grain-size distribution parameters. As suggested by Weingartner & Draine (2001), the grain-size distribution parameter sets with relatively large C abundance per H nucleus (b_c) are favored, which can better fit the extinction curve 2175 Å hump. We use the "LMC avg," "LMC 2," "SMC bar," "MW, $R_V = 3.1$," "MW, $R_V = 4.0$" and "MW, $R_V = 5.5$" models with b_c values 2.0×10^{-5}, 1.0×10^{-5}, 0, 5.58×10^{-5}, 4.72×10^{-5}, and 4.26×10^{-5}, respectively, in which the MW models' b_c values are adjusted (Draine 2003a, 2003b) from the original Weingartner & Draine (2001) b_c values. The size distributions of the six dust models are shown in Figure 4. For MW dust, the models with larger R_V have a larger portion of large-sized particles.

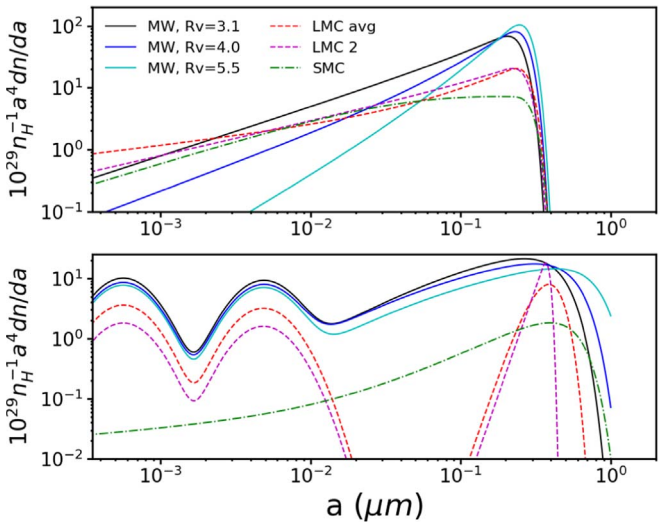

Figure 4. WD01 dust model size distributions. In the plot, the size distributions are weighted by a^4 for visualization purposes, where a is the grain size. Upper plot: silicate particle. Lower plot: carbonaceous particle.

The spectral optical properties including C_{ext}, SSA, and asymmetry factor (g) from ultraviolet (UV) to near-infrared (NIR) are shown in Figure 5. From red to NIR wavelengths, "MW, $R_V = 5.5$," "LMC avg," and "LMC 2," have very similar SSA and g, which are larger than those of other models.

In the computation, we specify the optical thickness or optical depth (τ) at one wavelength λ_0, and use the following equation to obtain the optical thickness at other wavelengths:

$$\tau(\lambda) = \frac{C_{ext,\lambda}}{C_{ext,\lambda_0}} \tau(\lambda_0). \quad (2)$$

Because the WD01 dust models do not provide full scattering phase matrix data, we use the Henyey–Greenstein (H-G) phase function (Henyey & Greenstein 1941) with the WD01 asymmetry factor data. A Rayleigh scattering phase matrix is utilized to simulate polarization, by keeping F_{ij}/F_{11} ($i, j = 1, 2, 3, 4$) unchanged and replacing F_{11} with the H-G phase function, where F_{ij} are the scattering phase matrix elements.

2.3. Comparison with Light-curve Observation

We compare MCRTM simulations with the OGLE-IV OTDS I-band light-curve observation of AT 2019xis. The AT 2019xis I-band light-curve data are downloaded from the

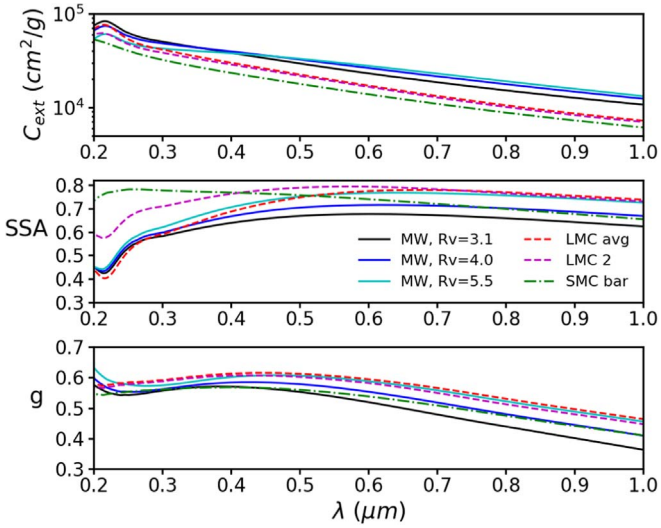

Figure 5. WD01 interstellar dust optical properties.

OGLE-IV OTDS website (http://ogle.astrouw.edu.pl/ogle4/transients). OGLE-IV is the fourth phase of the OGLE sky survey project (Udalski et al. 2015). The OGLE-IV OTDS is one of the OGLE-IV services aiming at observing SNe and other transients in the Magellanic Cloud Systems (Kozłowski et al. 2013; Wyrzykowski et al. 2014). The OGLE-IV observation is carried out by a 1.3 m Warsaw telescope at the Las Campanas Observatory, Chile. This telescope is equipped with a 32 CCD camera (Udalski et al. 2015). The OGLE-IV uses two filters of the Johnson–Cousins *I* and *V* bands. The observation cadence for LMC is around 5 days. The detectable *I*-band magnitude can be as faint as 22. Data reduction is conducted near-real time at the telescope site and then the reduced data are fed into the OGLE photometric pipeline (Wyrzykowski et al. 2014). The photometry of ongoing transients is available at the above-mentioned website, where the *I*-band magnitude is roughly calibrated within 0.2 (Wyrzykowski et al. 2014).

The OGLE-IV OTDS *I* band has a center wavelength of around 0.8 μm. The simulations are performed from 0.2 to 1.0 μm at wavelengths in WD01 data. The band-averaged Stokes vector is computed using

$$\bar{\boldsymbol{I}} = \frac{\int T(\lambda)\boldsymbol{I}(\lambda)d\lambda}{\int T(\lambda)d\lambda}, \tag{3}$$

where T is filter transmission and $\boldsymbol{I}$ is the Stokes vector.

In our MCRTM computations, the photons are emitted at one single time so the results are equivalent to an impulse response with a Dirac delta function as the input SN light curve. To compare with the observed AT 2019xis LE light curve, we need to consider SN 1987A light curves as the input. The simulated SN 1987A LE Stokes vector is a convolution between the impulse-response Stokes vector and the SN 1987A light curve, expressed as

$$\bar{\boldsymbol{I}}_{\rm LE}(t) = \int \bar{\boldsymbol{I}}(t-t')\bar{F}_{\rm SN}(t')dt', \tag{4}$$

where $\bar{\boldsymbol{I}}_{\rm LE}$ is the simulated LE Stokes vector and $\bar{F}_{\rm SN}$ is the SN flux at a specific band. The SN 1987A light-curve data are obtained from the first 500 days' photometric observation of SN 1987A at the Sutherland field station of South African Astronomical Observatory (Catchpole et al. 1987, 1988, 1989; Menzies et al. 1987; Whitelock et al. 1988) and downloaded from Open Supernova Catalog (OSC; Guillochon et al. 2017).[3] The observed *UBVRI* light curves are shown in Figure 6.

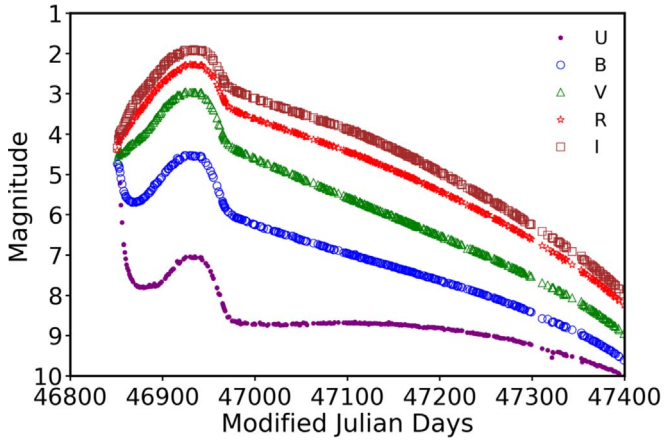

Figure 6. SN 1987A *UBVRI* light curves.

The parameters $l_{\rm ds}$, $d_{\rm ds}$, and $\theta_{\rm ds}$ in Figure 3 can be determined if we know the light delay time t_d and the angular distance between AT 2019xis and SN 1987A $\alpha_{\rm ds}$, both of which are measured at Earth. $l_{\rm ds}$, $d_{\rm ds}$, and $\theta_{\rm ds}$ have the following geometric relation:

$$(l_{\rm SN} - d_{\rm ds})\tan\alpha_{\rm ds} = l_{\rm ds}\sin\theta_{\rm ds}, \tag{5a}$$

$$ct_d = l_{\rm ds} - d_{\rm ds}, \tag{5b}$$

where $l_{\rm SN}$ is the distance between Earth and SN 1987A, and $\alpha_{\rm ds}$ (arcminutes) is determined by the coordinates of SN 1987A (R.A. 05:36:13.700 decl. −69:16:24.70) and AT 2019xis (R.A. 05:35:27.989 decl. −69:16:11.50). The delay time t_d is about 32.65 yr according to observed dates of SN 1987A and AT 2019xis. We use cross correlation between observed and simulated LE light curves to obtain a more accurate t_d. $\theta_{\rm ds}$ and $l_{\rm ds}$ are thus determined to be 18.9° and 186.3 pc, and t_d is computed to be 32.88 yr, with the difference from 32.65 yr probably resulting from imprecision in all measurements and computations.

We also estimate the dust cloud geometric size and optical thickness from the observed AT 2019xis light curve in the next section. We use the following cost function:

$$J = [L_{\rm obs} - L_{\rm sim}(\tau, r)]^T \boldsymbol{S}_\epsilon^{-1}[L_{\rm obs} - L_{\rm sim}(\tau, r)], \tag{6}$$

where r is the characteristic size of the dust clump, L is the light-curve magnitude, and $\boldsymbol{S}_\epsilon$ is the covariance matrix of observational errors. Here $\boldsymbol{S}_\epsilon$ is assumed to be a diagonal matrix with measurement uncertainty as the diagonal elements. We use the Levenberg–Marquardt method (Rodgers 2000) to minimize the cost function J and obtain the best-fit τ and r.

3. Results

The simulation assumes two cloud geometries, namely a spherical cloud and cube-shaped cloud. Apparently, neither shape is a realistic shape for the dust cloud as shown in Figure 2, but they are selected to study the sensitivity of an LE to the dust cloud shape. For the cube shape, one face of the

[3] https://sne.space

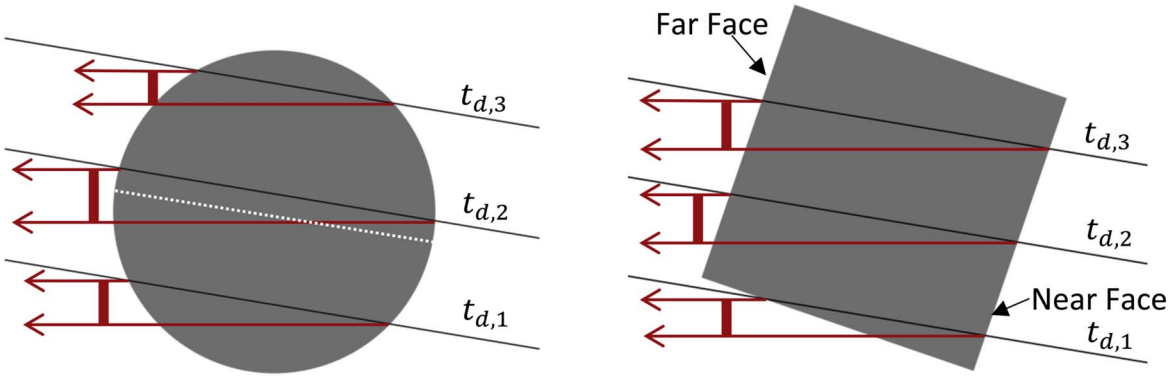

Figure 7. Two-dimensional views (yz plane, consistent with Figure 3) of the dust cloud shapes used in the MCRTM simulation. The black curves are light echo parabolas corresponding to three delay times $t_{d,1}$, $t_{d,2}$, and $t_{d,3}$. $t_{d,1} < t_{d,2} < t_{d,3}$. The red arrows are along the line of sight toward the observer. The red rectangles denote the areas where the dust cloud is illuminated at a single delay time. Left plot: a spherical dust cloud. The white dashed line denotes a great circle of the sphere. Right plot: a cube-shaped dust cloud. The annotated Near Face and Far Face are two faces of the cube perpendicular to the yz plane.

cube is perpendicular to the straight line formed by SN 1987A and the geometric center of the cube. A 2D view of the two dust cloud shapes overlapping with the parabola model is shown in Figure 7. If the light source is an impulse, the singly scattered LE can be predicted using the paraboloid model.

As shown in Figure 7, the simulated impulse response of singly scattered light will be observed as a bright strip with a certain width at a single delay time. The shape of the observed bright strip is determined by the dust cloud shape. For a spherical shape, the length and width of the strip keep increasing until the LE paraboloid intersects the great circle of the sphere. Then, the length and width of the strip start to decrease. For a cube, because of the orientation of the cube, the length of the bright strip will almost be a constant. The width of the bright strip increases until the LE paraboloid intersects both the Near Face and Far Face annotated in Figure 7. Then, the width of the strip is a constant until the LE paraboloid does not intersect the Near Face, and the width then starts to decrease. The variation of the LE shape will be reflected in the light-curve shape. When the light curve of the source SN is included and multiple scattering is considered, the LE variation will be more complicated.

3.1. Light-curve Simulations

We use the MCRTM to simulate LE light curves of SN 1987A at the AT 2019xis position under a variety of dust cloud properties including optical thickness, dust grain model, dust cloud size, and dust cloud shape. The dust cloud is assumed to be homogeneous so the extinction coefficient in Equation (B4) is a constant. The simulated light curves are shown in Figures 8–11.

In Figure 8, only optical thickness is a variable. The dust cloud is assumed to be a sphere with diameter 1.8 lt-yr and is composed of "LMC avg" dust properties. The simulated light curves can roughly capture the observed light-curve shape when the diameter optical thickness is smaller than 4. The light-curve maxima of the optically thin cases ($\tau < 4$) arrive later than the optically thick cases. Because the dust grains are absorptive, when the dust cloud is optically thick, only areas close to the cloud surface have light come to the observer, so after the light-curve maximum, the LE luminosity decreases fast. In an optically thin cloud, the light scattered deeply into the cloud can come out of the surface and be

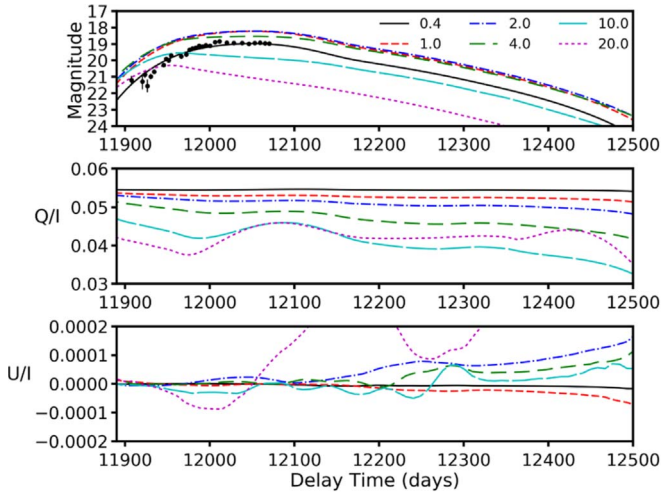

Figure 8. Simulated SN 1987A I-band light echo light curves and associated Q and U components of Stokes vector with varied diameter optical thickness at 0.8 μm wavelength. The dust cloud is assumed to be a sphere having diameter 1.8 lt-yr. The "LMC avg" dust model is used in the simulation. The black dots are the AT 2019xis I-band observations by OGLE-IV OTDS.

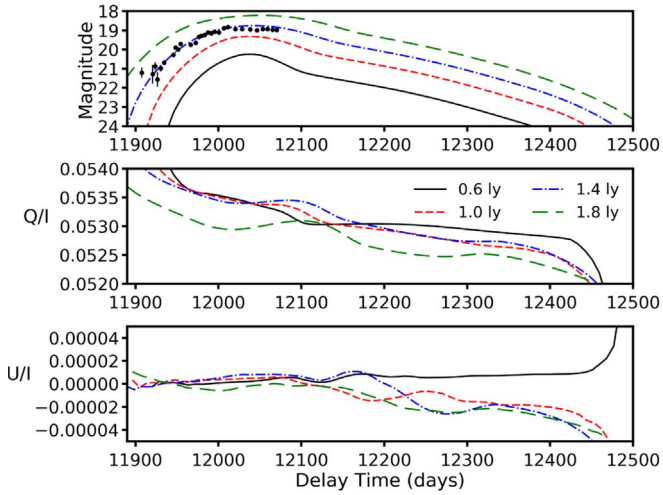

Figure 9. The same as Figure 8, but with varied dust cloud sphere diameters. The diameter optical thickness at 0.8 μm wavelength is 1.0.

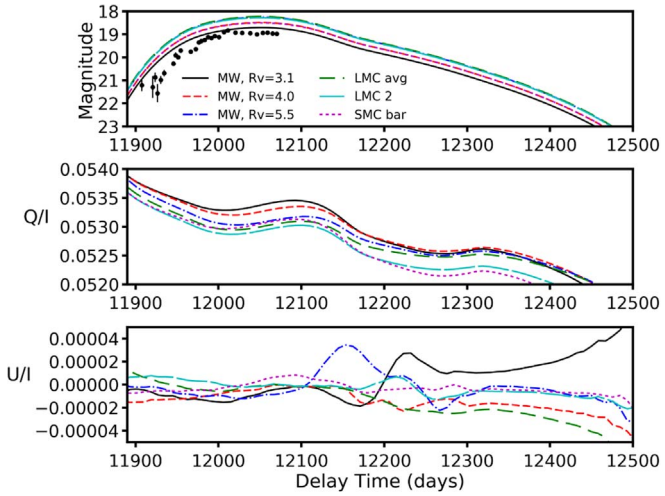

Figure 10. The same as Figure 8 but with varied dust models. The dust cloud has a diameter optical thickness at 0.8 μm wavelength of 1.0 and diameter 1.8 lt-yr.

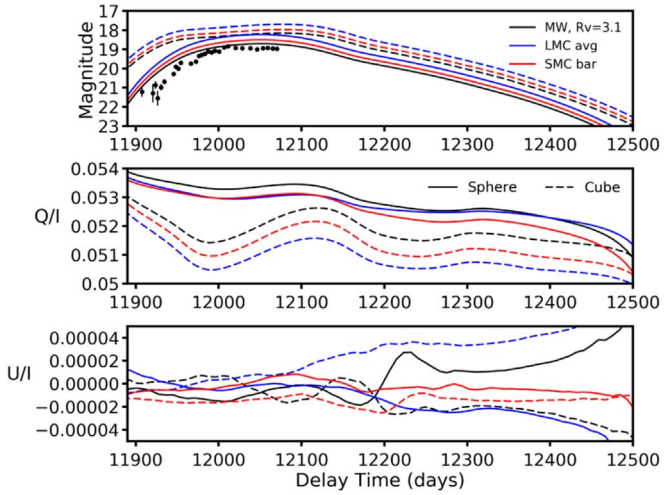

Figure 11. The same as Figure 8, but with three dust models and two dust cloud shapes. The spherical dust cloud, of 1.8 lt-yr diameter, has optical thickness 1.0 along a diameter at 0.8 μm wavelength. The cube-shaped dust cloud, with side length 1.8 lt-yr, has optical thickness 1.0 along a side at 0.8 μm wavelength. Solid lines denote spherical dust clouds, and dashed lines denote cube-shaped dust clouds.

observed, so after the light-curve maximum, the LE luminosity decreases slowly. At the same delay time, the LE luminosity increases with increased optical thickness up to 2 and then decreases with further increased optical thickness. When the dust cloud is optically thin, if optical thickness increases moderately, more light is scattered to the observer. However, if optical thickness increases to a value where absorption is significant, light scattered to the observer would decrease. Thus, the LE luminosity does not increase monotonically with increased optical thickness.

The linear polarization degree p_l and angle χ are defined as

$$p_l = \frac{\sqrt{Q^2 + U^2}}{I}, \tag{7}$$

$$\chi = \frac{1}{2}\arctan\left(\frac{U}{Q}\right), \tag{8}$$

where χ is the angle between the linear polarization plane and a reference plane. As shown in Figures 8–11, the Q component of the LEs Stokes vector is always positive and the U component is close to zero, which indicates that the preferential linear polarization direction is parallel to the polarization reference plane, the xz plane in Figure 3. If the dust cloud and SN 1987A are treated as points, the scattering plane is the yz plane. Thus, the preferential linear polarization direction is perpendicular to the scattering plane. The linear polarization degree decreases with increased optical thickness.

Figure 9 shows the effect of dust cloud diameter on the LE. When the optical thickness is held constant, a larger dust cloud has a stronger LE. Because a larger dust cloud receives more light from the source, more light is scattered to the observer if the optical thickness is unchanged. The linear polarization is not sensitive to the dust cloud size. As shown in Figure 9, the variation of linear polarization is smaller than 0.1%.

Figure 10 shows that the dust cloud LE is sensitive to dust optical properties. "MW," $R_V = 5.5$, "LMC avg," and "LMC 2" have similar LE light curves. These three dust models have similar SSAs and asymmetry factors in the I band. "MW, $R_V = 4.0$" and "SMC bar" also have very similar SSAs and asymmetry factors, and their light curves are almost identical. The simulated linear polarization is not very sensitive to dust optical properties, because we have assumed that the six models have the same polarization property in Section 2.2.

In Figure 11, we compare light curves of two dust cloud shapes, namely a sphere and a cube. The shapes of light curves by a spherical and a cube-shaped dust cloud are significantly different before the light-curve maxima. The light curve before the maximum of a cube-shaped dust cloud is like a line segment whereas that of a spherical dust cloud has obvious curvature. The linear polarization of the two dust cloud shapes is also different, though not substantially.

We also simulate LE light curves of the dust cloud in the U, B, V, and R bands, where the Johnson–Cousins filters (Landolt 2009) are used. The optical thickness is 1.0 along a diameter at 0.8 μm wavelength and the U-, B-, V-, and R-band optical thicknesses are larger according to Figure 5 and Equation (2). The simulated U, B, V, R and I band light curves are shown in Figure 12. Besides the optical thickness, the input SN 1987A light curves and dust optical properties also vary greatly in these five bands, so the LE light curves have a strong band dependence.

3.2. Simulated LE Images

In this subsection, we show the LE images simulated by the MCRTM. For illustrative purposes, we also show the impulse response of the corresponding scattering event, where the SNe light curve is modeled by a Dirac delta function. Figures 13 and 14 show the simulated U-band and I-band LE images at different delay times. The optical thickness in the I band is small (1.0 at 0.8 μm wavelength). The corresponding optical thickness at 0.365 μm is about 3.2 so the U band has a larger optical thickness.

As shown in Figures 13 and 14, after the I-band light-curve maximum, the whole dust cloud is illuminated for a while. A bright horizontal strip is caused by the SN 1987A I-band light-curve maximum as shown in Figure 6. In the corresponding impulse response, the bright horizontal strip is narrow and there is almost no light outside the strip. According to the analysis

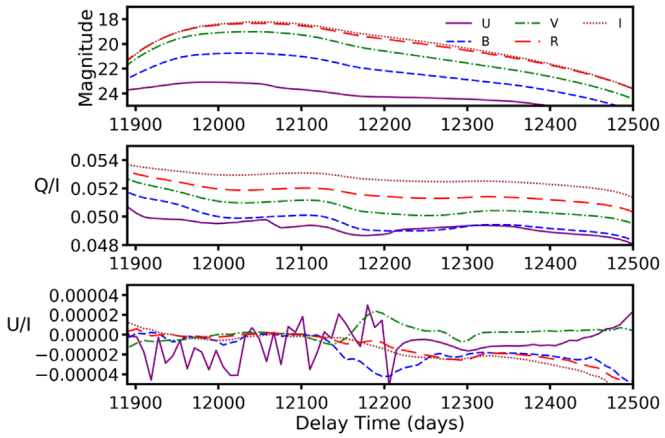

Figure 12. The same as Figure 8, but for different spectral bands (the same as in Figure 6). The spherical dust cloud with diameter 1.8 lt-yr has optical thickness 1.0 along a diameter at 0.8 μm wavelength (I band), increasing to about 3.2 at 0.365 μm (U band). The LMC avg dust model is assumed.

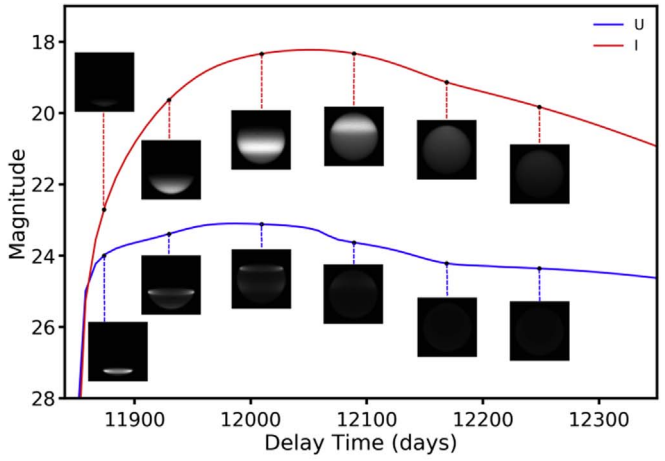

(a)

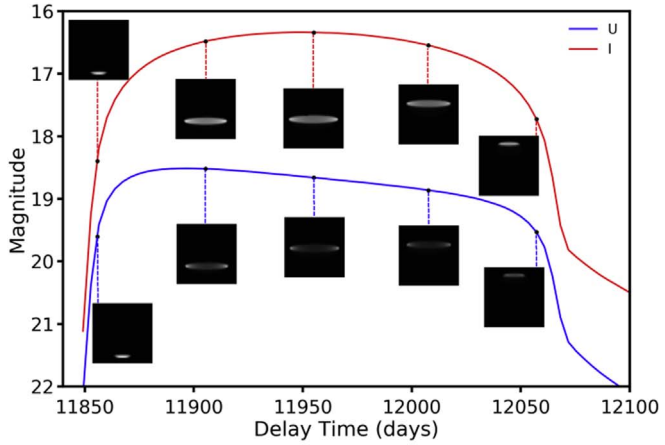

(b)

Figure 13. Simulated SN 1987A I-band and U-band light echo light curves and images at several delay times. The dust cloud is assumed to be a sphere having diameter 1.8 lt-yr. The diameter optical thickness at 0.8 μm wavelength is 1.0. The LMC avg dust model is used in the simulation. For either band, the same colormap is used to plot all grayscale images in this band, but the colormaps used for the I and U bands are different. (a) SN 1987A light curve is used in the simulation; (b): a Dirac delta function multiplied by the maximum flux of SN 1987A photometry is the SN's light curve in the simulation.

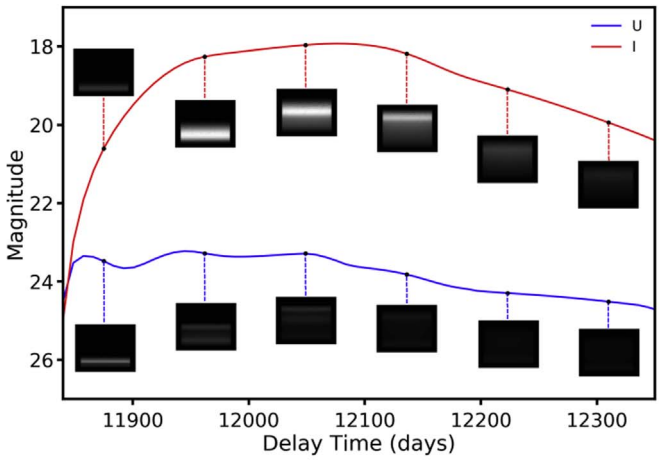

(a)

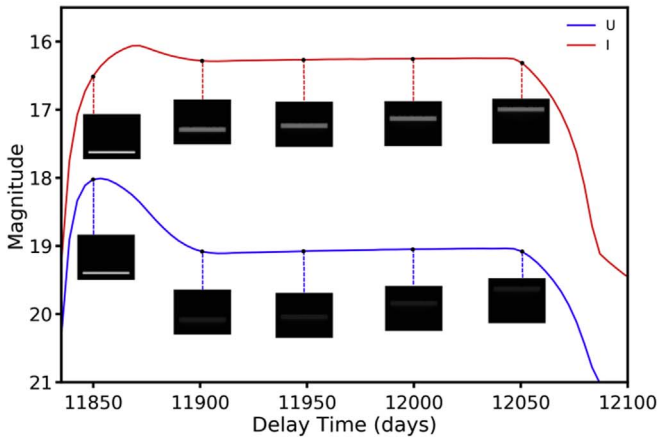

(b)

Figure 14. The same as Figure 13 but for a cube shape. The side length is 1.8 lt-yr. The side optical thickness at 0.8 μm wavelength is 1.0.

using Figure 7, the single-scattering contribution is very significant. The bright strip first appears at the bottom of the dust cloud, then moves upward with time and finally disappears at the top. The movement of the bright strip is consistent with the upward-moving LE paraboloid. Because of the position of the dust cloud and SN 1987A, for a spherical dust cloud, the light observed at the top of the cloud experiences a longer distance within the dust cloud than at the bottom and thus is dimmer. This phenomenon is very obvious in the I-band images in Figure 13. The light-curve maximum appears at the time when the strip just passes the center of the dust cloud. In contrast, for a cube-shaped dust cloud, the singly scattered LE has the same travel distance in the dust cloud. Thus, the bright strip of the LE has almost the same brightness when moving from the bottom to the top of the dust cloud.

Because the U-band and I-band light-curve maxima of SN 1987A are almost synchronous, a bright strip appears in the same position in the U-band image as in the corresponding I-band image. In addition to the bright strip coinciding with that in the I-band image, a much brighter and narrower strip appears ahead of the dimmer strip, which is very similar to the bright strip of the corresponding impulse response. This brighter strip is caused by the shock breakout following shortly after the SN 1987A explosion. The U-band light curve of SN 1987A in

Figure 6 shows the fading of the UV-bright shock breakout, which is strong and lasts a very short time so the LE caused by the UV shock breakout is close to an impulse response. In the *U* band, the optical thickness is large. For a spherical dust cloud, most of the observed light is concentrated close to the dust cloud surface because that region experiences less extinction. In the *U*-band LE image in Figure 13, the bright strip is dim in the center and bright at its two ends. This inhomogeneous bright strip brightness is not shown in the *U*-band LE image for a cube-shaped dust cloud, because the light has the same extinction across its bright strip.

The *U*-band light curve is flatter than the *I*-band light curve around the maximum as shown in Figures 13 and 14 and in Figure 12. The impulse-response light curves and images in the lower plots of Figures 13 and 14 can explain the *U*-band flat light curves. In the *U* band, the LE of the strong UV-bright shock dominates the received signal so its light-curve shape resembles the corresponding impulse response, which is flat when the bright strip moves from one side of the dust cloud to another side. For an impulse response, the magnitude of the LE is proportional to the dust volume that the LE paraboloid intersects.

In the lower plots of Figures 13 and 14, the area and brightness of the bright strip determine the LE magnitude. In other words, the impulse-response light curve depicts the shape of the dust cloud. For a spherical dust cloud, the *I*-band impulse-response light curve is almost symmetric with respect to the maximum because the *I*-band extinction is weak. In contrast, the *U*-band impulse-response light curve looks like a symmetric light curve multiplied by an attenuation term that increases with the delay time. Based on the left plot of Figure 7, when the bright strip moves from the bottom to the top of the spherical dust cloud, the average path length of photons in the dust cloud is longer so the dust extinction is stronger in both *U* and *I* bands. The *U*-band optical thickness is larger than in the *I* band, so the decreasing trend in the *U*-band light curve is more obvious. For a cube-shaped dust cloud, the *I*-band and *U*-band impulse-response light curves have similar shapes. The LE magnitude gradually reaches its maximum in the stage where the width of the bright strip increases. Then, the light curve decreases to a point and becomes flat with a slightly increasing trend. In this stage, the width of the bright strip is constant and the path length of singly scattered photons in the dust cloud at various delay times is the same. The slight increasing trend is attributed to multiple scattering. Later on, the impulse-response light curve starts to decrease, which coincides with the decreasing bright strip width. In short, the light-curve shape of the impulse response is a combined result of dust cloud shape and extinction.

Figure 15 shows the simulated *I*-band LE images when the dust cloud is optically thick. For a spherical dust cloud, the LE looks like an incomplete ring because only the light scattered by the sphere's surface is observable. At the light-curve maximum, the incomplete ring is less than 180° when the SN 1987A *I*-band light-curve maximum has not passed the center of the sphere yet. This explains why the light-curve maximum of an optically thick cloud appears earlier than an optically thin cloud. For a cube-shaped dust cloud, only the light scattered by the bottom surface is observable. Because a cube is a faceted shape and four faces are parallel to the incident light, the left and right surfaces of the cube-shaped

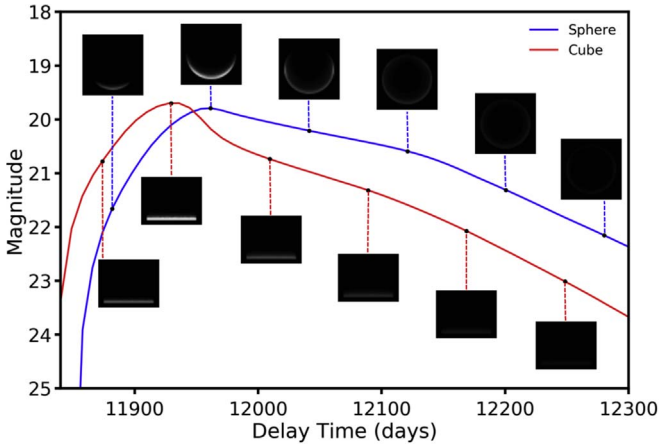

Figure 15. Simulated SN 1987A *I*-band light echo light curves and images at six delay times for a spherical and a cube-shaped dust cloud shape. The spherical dust cloud has diameter 1.8 lt-yr and diameter optical thickness 10.0 at 0.8 μm wavelength. The cube-shaped dust cloud has side 1.8 lt-yr and side optical thickness 10.0 at 0.8 μm wavelength. The "LMC avg" dust model is used in the simulation. For each dust cloud shape, the same colormap is used to plot all grayscale images. The colormaps used for spherical and cube-shaped dust clouds are different.

dust cloud in Figure 15 cannot scatter light toward the observer. The regions adjacent to the left and right surfaces are optically thick along the observation direction. Therefore, the observer can only see the LE at the cube's bottom region.

Figures 16–18 give zoomed views and linear polarization patterns at a single delay time of the LE images in Figures 13–15, respectively. In Figures 16 and 17, the LE illuminates the whole dust cloud. The linear polarization pattern does not vary substantially in an *I*-band LE. The linear polarization degree is around 5%, and the preferential polarization direction is generally perpendicular to the *yz* plane. In a *U*-band LE, the linear polarization degree around the center is smaller than that adjacent to the surface. In some areas, the preferential polarization direction is not perpendicular to the *yz* plane, which indicates the *U* Stokes parameter values in these areas are nonzero.

Because the dust clouds in our simulations are homogeneous and symmetrical about the incident direction, the simulated LEs are also symmetrical about the incident direction if the Monte Carlo noise is excluded. The *U* Stokes parameter of a point at one side of the axis of symmetry should have the same magnitude as but opposite sign to its symmetric point on another side of the axis of symmetry. Therefore, as shown in Figures 8–12, the averaged *U* Stokes parameters are nearly zero, although they may not be zero everywhere on the LE.

For the optically thick case in Figure 18, most unilluminated regions have zero polarization. In illuminated regions of the spherical dust cloud, the preferential polarization direction is radial, which is perpendicular to the local scattering plane that is parallel to the sphere surface. Because the dust cloud is optically thick, observable light must go through a very short path in the dust. Only light scattered by the dust cloud surface satisfies the short-path condition. Because almost all of the observed light goes through a very short path in the dust, singly scattered light dominates the observation. Therefore, the linear polarization degrees in some regions are up to 10% and the preferential polarization directions are along radial directions. The top of the spherical dust cloud is dim but has horizontally

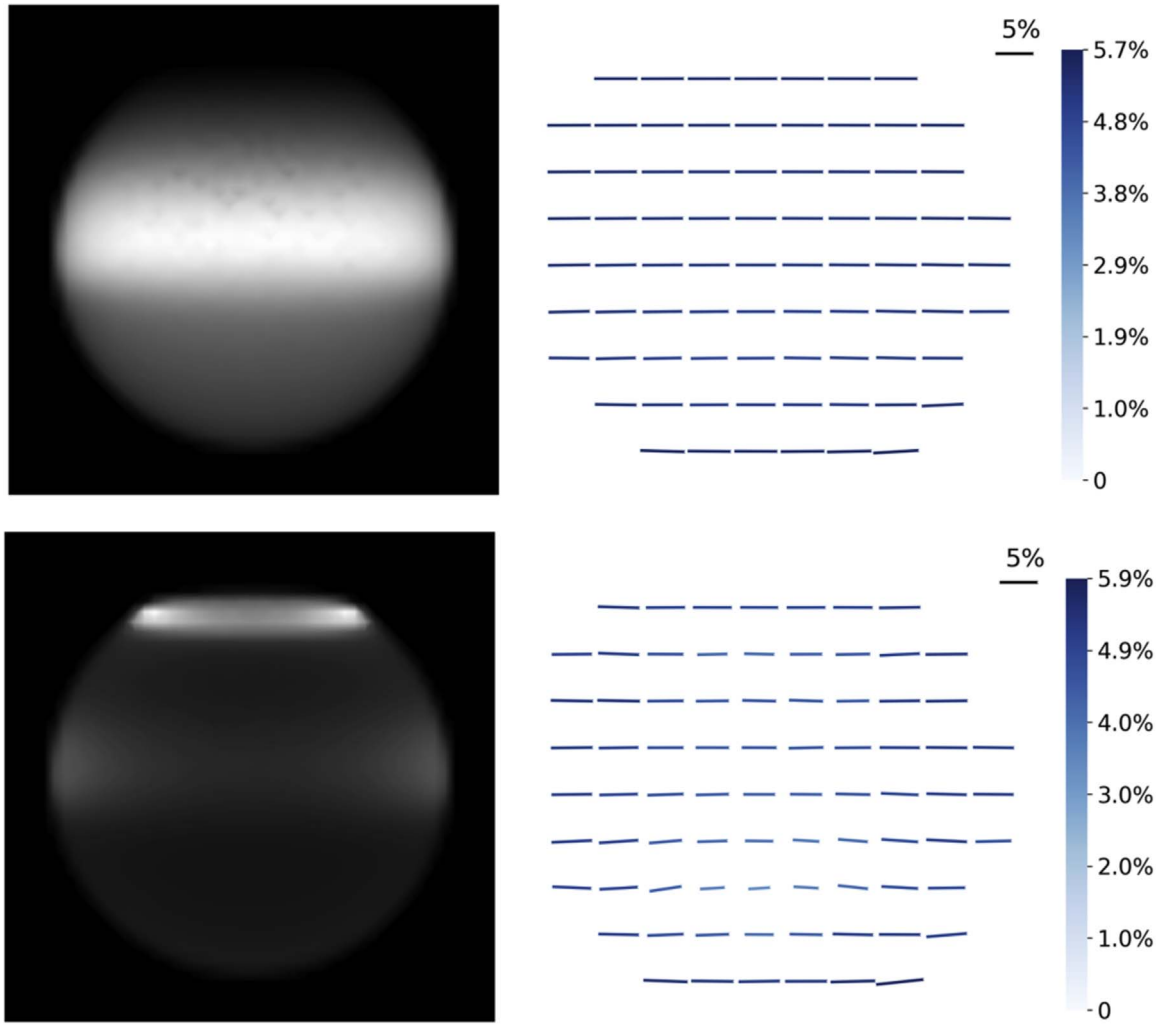

Figure 16. Simulated SN 1987A *I*-band and *U*-band light echo images and linear polarization patterns. The dust cloud is the same as in Figure 13. Top row: *I* band. Bottom row: *U* band. Left column: simulated light echo images. Right column: simulated linear polarization patterns. The length and color of the line segments in linear polarization patterns indicate the linear polarization degree defined in Equation (7). The "5%" marker denotes linear polarization degree 5%. The pointing direction of a line segment forms an angle with the right horizontal direction, which is the polarization angle defined in Equation (8). The two grayscale images use different colormaps.

distributed linear polarization, which is weaker than the radially distributed counterpart below. This horizontally distributed linear polarization is dominated by multiple scattering, which tends to reduce polarization.

3.3. Estimation of Dust Cloud Size and Optical Thickness

We use the MCRTM simulations to fit the OGLE-IV OTDS *I*-band light curve and estimate the dust cloud size and optical thickness. The best-fit light curves are shown in Figure 19. Table 1 lists the estimated dust cloud size and optical thickness.

All the best-fit light curves fit the overall shape of the observed light curve well but none of them captures the local minima and maxima before and after a delay time of 11,980 days. Our simulations assume that the dust cloud has simple and regular shapes but the realistic dust cloud is irregular and inhomogeneous, as shown in Figure 2. The complex shape and inhomogeneity result in the observed light curves local minima and maxima.

After a delay time of 11,980 days, the light curves gradually become flat. After a delay time of 12,060 days, the observed light curve tends to decrease. Because we do not have more observations, we are not sure if this decrease is a local minimum or a decreasing trend of the light curve after a global maximum. As shown in Table 1, the estimated dust cloud size and optical thickness by "MW, $R_V = 3.1$," "MW, $R_V = 4.0$," and "SMC bar" dust models are larger than the two LMC dust models. The "MW, $R_V = 5.5$" model has larger optical thickness but smaller size than the LMC dust models. We find in Section 3.1 that, at the same delay time, the LE magnitude is larger for a larger dust cloud if the optical thickness is unchanged. For any dust cloud size and the same delay time, there is a maximum achievable LE magnitude. The maximum achievable LE magnitude is determined by the dust cloud absorption capability and size. A more absorptive dust cloud scatters less light and therefore has a smaller maximum achievable LE magnitude. The "MW, $R_V = 3.1$," "MW, $R_V = 4.0$" and SMC bar" models have smaller *I*-band SSAs and thus are more absorptive than the other three models. Thus, to generate a light curve fitting the observed light curve, the dust cloud size of the "MW, $R_V = 3.1$," "MW, $R_V = 4.0$," and SMC bar models must be larger than those of other models.

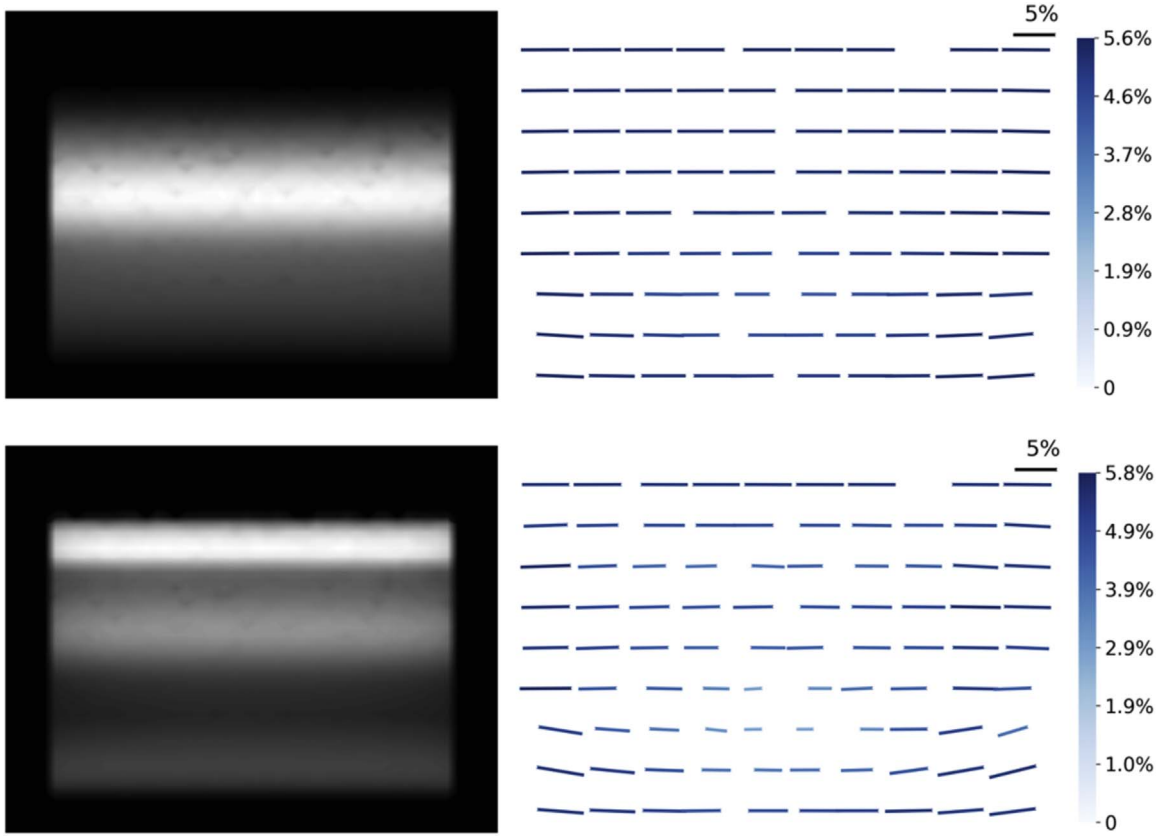

Figure 17. The same as Figure 16, but for the dust cloud defined in Figure 14.

The mass of the dust cloud can be computed using the estimated cloud size and optical thickness,

$$M = \frac{\pi D^2 \tau_D}{6 C_{\rm ext}}, \tag{9}$$

for a spherical dust cloud, and

$$M = \frac{a^2 \tau_a}{C_{\rm ext}}, \tag{10}$$

for a cube-shaped dust cloud. D is diameter and τ_D is the optical thickness along a sphere diameter. a is side length and τ_a is the optical thickness along a cube side. The estimated mass data are listed in Table 1. Except for "MW, $R_{\rm V} = 5.5$" model, the estimated mass from assuming a spherical shape is slightly smaller than that by assuming a cube shape if the same dust model is used, which indicates that the dust cloud shape assumption does not significantly affect the mass estimation result.

If we assume a gas-to-dust ratio of 300, which is within the reported gas-to-dust ratio range in the LMC (e.g., Roman-Duval et al. 2014), and use the minimum and maximum estimated dust masses with the two LMC dust models, the total mass of the cloud is about 7.8–9.3 $M_\odot$. If we consider either homogeneous spherical or cube-shaped cloud, the cloud mass is estimated to be 7.8–8.4 $M_\odot$ or 8.1–9.3 $M_\odot$ respectively. If we assume the dust has MW dust optical properties, the estimated mass is 7.2–29.0 $M_\odot$ and 8.4–16.3 $M_\odot$ for spherical and cube-shaped clouds, respectively. The dust optical property uncertainty is comparable to the cloud shape uncertainty. Furthermore, the estimated mass ranges have similar smallest values but very different largest values. This implies that according to radiative transfer calculation, the scattered flux at the I band is not sensitive to optical thickness variation when the optical thickness is large.

With the best-fit dust cloud optical thickness and size, we can simulate the LE in other unobserved bands. Here we take Swift (Gehrels et al. 2004) UV/Optical Telescope (UVOT) (Roming et al. 2005) as an example to simulate the LE light curves in six UVOT filters (*v, b, u, uvw1*, *uvw2*, and *uvm2*). The UVOT filter effective area data and zero points in the Vega system (Breeveld et al. 2011) are obtained from the SVO Filter Profile Service (Rodrigo et al. 2012; Rodrigo & Solano 2020).[4] To calculate the brightness of the LE in the (unobserved) UV, we use UV spectra from the International Ultraviolet Explorer (IUE) published by Pun et al. (1995). These IUE spectra were combined with optical spectra from Phillips et al. (1988, 1990). The combined spectra are available from the OSC (Guillochon et al. 2017) and the Weizmann Interactive Supernova Data Repository (WISeREP; Yaron & Gal-Yam 2012).[5] Low- or zero-flux gaps at the beginning, end, or between spectra were deleted, and the gaps between spectra were replaced with a linear interpolation.

The combined SN 1987A spectra are at 28 epochs ranging from −81 to 632 days relative to the date of B-band maximum (modified Julian day 46931.0). We construct the SN 1987A light-curve magnitude in the UVOT *v, b, u, uvw1, uvw2*, and

[4] http://svo2.cab.inta-csic.es/theory/fps/
[5] https://wiserep.weizmann.ac.il

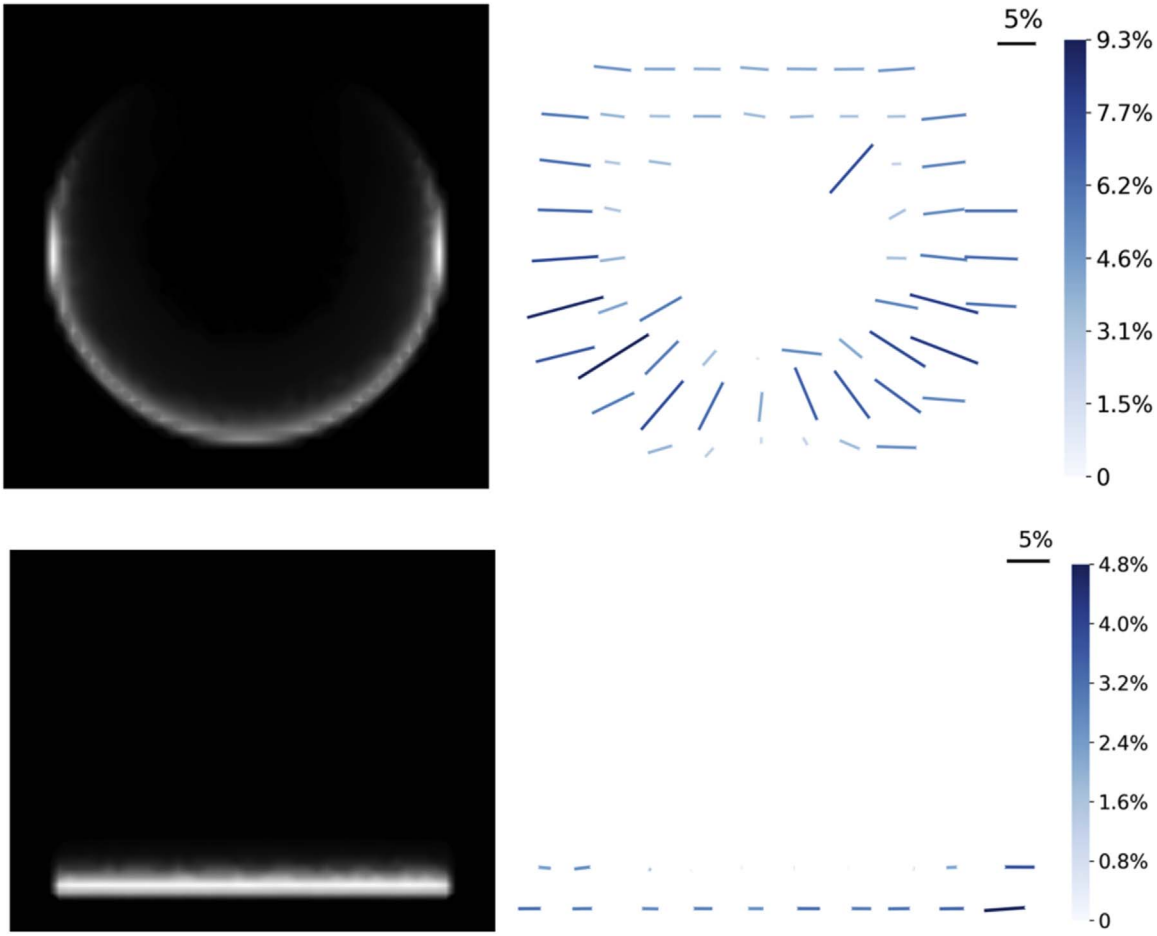

Figure 18. Simulated SN 1987A *I*-band light echo images and linear polarization patterns. The two dust clouds are the same as in Figure 15. Top row: spherical dust cloud. Bottom row: cube-shaped dust cloud. Left column: simulated light echo images. Right column: simulated linear polarization patterns. The length and color of the line segments in linear polarization patterns indicate the linear polarization degree defined in Equation (7). The 5% maker denotes a linear polarization degree of 5%. The pointing direction of a line segment forms an angle with the right horizontal direction, which is the polarization angle defined in Equation (8). The two grayscale images use different colormaps.

*uvm*2 bands using the formulas:

$$\bar{F} = \frac{\int T(\lambda)F(\lambda)d\lambda}{\int T(\lambda)d\lambda}, \tag{11a}$$

$$\mathrm{mag} = -2.5\log_{10}\left(\frac{\bar{F}}{F_0}\right), \tag{11b}$$

where $\bar{F}$ is band-averaged flux, $F(\lambda)$ is the flux at a single wavelength, F_0 is the Vega zero-point flux, and mag is the magnitude in Vega system. With the constructed flux $\bar{F}$ at a specific filter, we can calculate the LE brightness using Equations (3) and (4). Because we have SN 1987A UV spectra, we can calculate the LE brightness with a stricter approach. The LE flux is first computed wavelength by wavelength and then integrated with the filter transmission to get the band-averaged flux,

$$\bar{F}_{\mathrm{LE}}(t) = \int\int F_\delta(\lambda, t - t')F_{\mathrm{SN}}(\lambda, t')T(\lambda)d\lambda\, dt', \tag{12}$$

where $\bar{F}_{\mathrm{LE}}$ is the LE flux at a specific band, F_δ is the simulated impulse-response flux of the LE and F_{SN} is the SN spectral flux.

In the calculation, we pick the best-fit dust cloud optical thickness and size in Table 1 with the assumption of "LMC avg" dust model and spherical cloud shape. The results are shown in Figure 20. The simulated UVOT *v*- and *b*-band light-curve shapes are similar to the *V*- and *B*-band light curves in Figure 12. The strong and short UV-bright shock breakout makes the LE UV light curves close to the impulse response as explained in Section 3.2. The LE light curves are calculated with two approaches. One is consistent with Equations (3) and (4), and another is stricter using Equation (12). As shown in Figure 20, in the *v* and *b* bands, the results using the two approaches are almost identical. In the UV bands, especially *uvw*1 and *uvw*2, the light-curve differences computed by the two approaches are substantial. This is because the interstellar dust optical properties have a more significant spectral dependence in the UV wavelengths. As shown in Figure 5, the dust SSA has a sharper variation with wavelength in UV. Thus, to accurately model LEs in UV, the UV spectra of SN are necessary.

The strong spectral dependence of UV dust optical properties does not impair the importance of obtaining SN 1987A early UV radiation information from the UV LE. The strong UV breakout at the early stage of SN 1987A explosion generates a UV LE close to the impulse response of the dust cloud. Because the SN 1987A *V*-band light curve does not have an early peak, the differences between the UV and *V*-band LE light-curve shapes contain information on the duration and

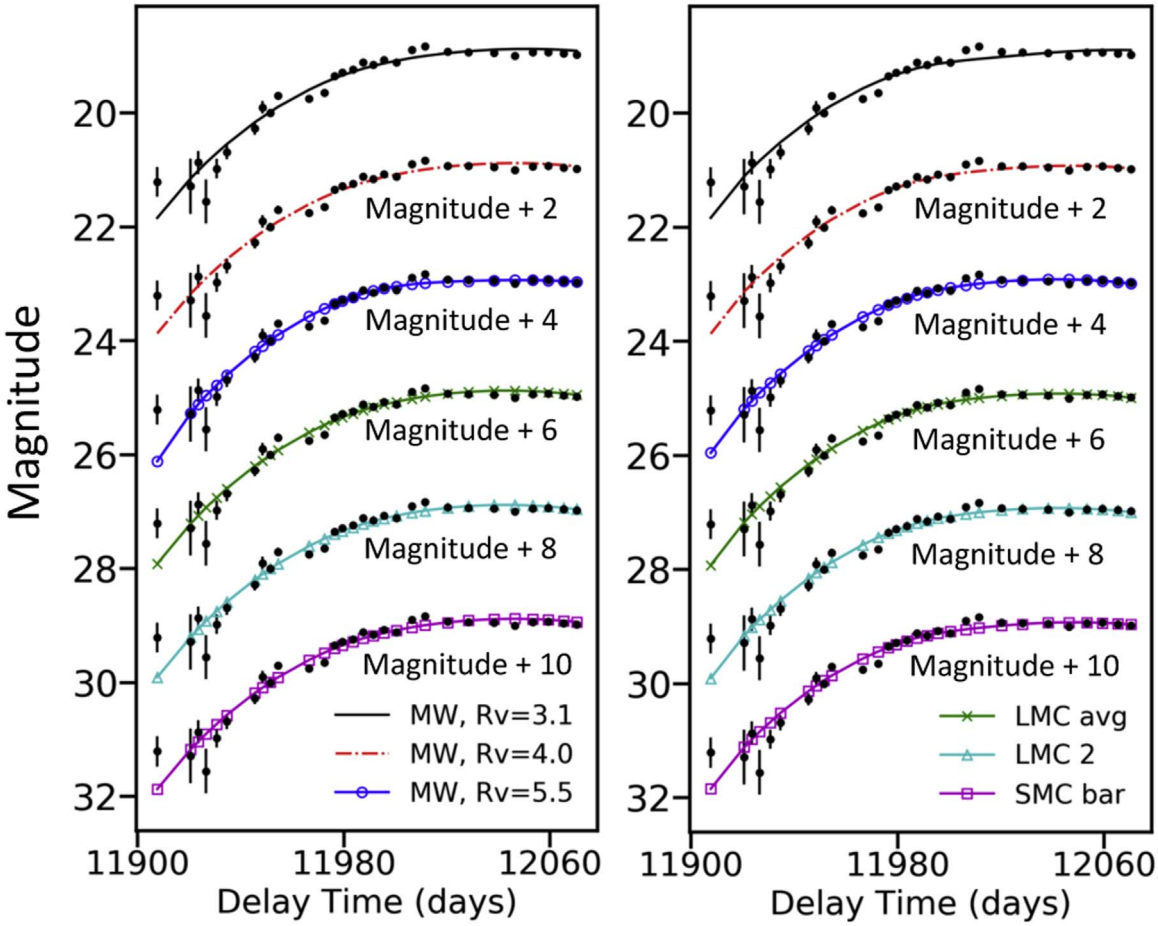

Figure 19. Best-fit simulated *I*-band light echo light curves to the OGLE-IV OTDS AT 2019xis observation using six dust models. The black dots are AT 2019xis *I*-band observations. Left: the dust cloud is assumed to be a sphere; Right: the dust cloud is assumed to be a cube. The magnitudes of "MW, $R_V = 4.0$," "MW, $R_V = 5.5$," "LMC avg," "LMC 2," and SMC bar are shifted for clarity.

Table 1
Best-fit Dust Cloud Size, Optical Thickness (τ), and Estimated Mass

Dust Model	Shape	Size[a] (lt-yr)	τ[b]	Mass ($M_\odot$)
MW, $R_V = 3.1$	Sphere	1.59	1.07	0.042
MW, $R_V = 4.0$	Sphere	1.54	0.74	0.024
MW, $R_V = 5.5$	Sphere	1.43	3.78	0.096
LMC avg.	Sphere	1.51	0.50	0.026
LMC 2.	Sphere	1.50	0.54	0.028
SMC bar	Sphere	1.54	0.69	0.044
MW, $R_V = 3.1$	Cube	1.32	1.03	0.053
MW, $R_V = 4.0$	Cube	1.16	0.82	0.028
MW, $R_V = 5.5$	Cube	1.11	0.59	0.017
LMC avg	Cube	1.12	0.51	0.027
LMC 2	Cube	1.11	0.56	0.031
SMC bar	Cube	1.17	0.82	0.057

Notes.
[a] For sphere, size is the diameter; for cube, size is the cube side length.
[b] For sphere, τ is along diameter; for cube, τ is along a cube side. All τ values are at 0.8 μm wavelength.

intensity of UV breakout. As shown in the inset plot of Figure 20, the early UV peaks at the *u* and *uvw1* bands are wider than at *uvw*2 and *uvm*2. This is reflected in the LE light curves. Although the largest values of the UV peaks are similar in the four UV bands, the light-curve plateau magnitudes at *u* and *uvw*1 are about two magnitudes larger than those at *uvw*2 and *uvm*2.

Further distinctive features can be measured if the echo can be spatially resolved. The echoes in the UV are in general much sharper than the echoes in the optical range and are located at the leading edges of the echoes.

4. Summary

In this study, we use an efficient MCRTM to simulate an SN 1987A LE, which was observed as AT 2019xis in the LMC, including light curves, LE images, and linear polarization. The theoretical simulations are compared with OGLE-IV OTDS light-curve observations and are used to estimate the properties of the dust cloud that produced the AT 2019xis LE.

HST images show that the dust cloud in AT 2019xis is a branch of a larger cloud and has a complicated shape. Because we do not know the exact shape of the dust cloud, for simplicity, we model the dust cloud as a homogeneous sphere or cube in simulations. The distance between the dust cloud and SN 1987A is estimated to be 186.3 pc using their angular distance and the delay time of the LE. The SSA and asymmetry factor data of the six WD01 dust models are used in the simulations. The H-G phase function and WD01 asymmetry factor data are combined to obtain the dust cloud's phase function or element (1, 1) of the scattering phase matrix. The ratios of other scattering phase matrix elements to the phase

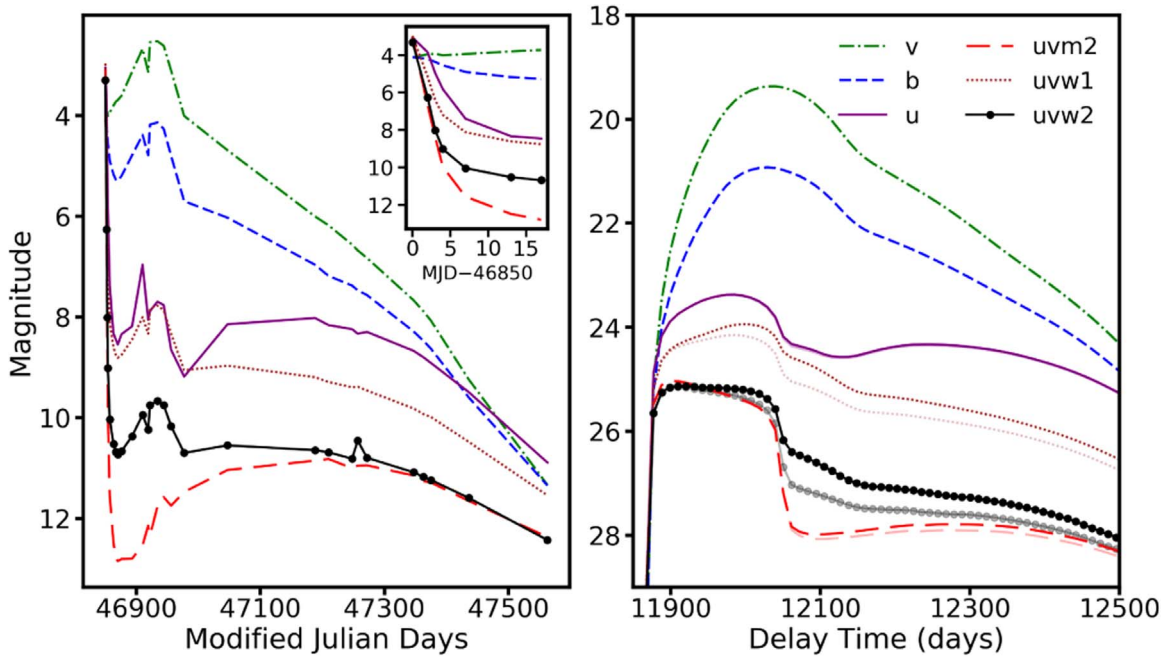

Figure 20. Left: constructed SN 1987A light curves in Swift UVOT *v, b, u, uvw1, uvw*2, and *uvm*2 bands using the combined SN 1987A spectra at 28 epochs. Right: the simulated light echo light curves in the six corresponding Swift UVOT filters. The dust cloud is assumed to be a sphere having diameter 1.51 lt-yr. The "LMC avg" dust model is used in the simulation. The diameter optical thickness at 0.8 μm wavelength is 0.5. The optical thicknesses at *v, b, u, uvw1, uvw*2, and *uvm*2 are about 0.95, 1.29, 1.65, 2.23, 3.53, and 3.45, respectively. Equation (12) is used to compute the light echo light curves. The corresponding curves with lighter colors are light curves computed by the approximated approach using Equations (3) and (4). The inset plot is a zoomed view of SN 1987A light curve 0–17 days from modified Julian day (MJD) 46850.

function are the same as with the counterpart of the Rayleigh scattering phase matrix.

The LE light-curve magnitude and shape are sensitive to the dust cloud size, shape, optical thickness, and dust grain optical properties. Because the dust cloud is absorptive, the light-curve magnitude is not monotonic with an increasing optical thickness. With all other conditions unchanged, at any delay time, the light-curve magnitude first increases with a larger optical thickness. If the optical thickness further increases, the light-curve magnitude starts to decrease. The LE light-curve maximum arrives earlier if a dust cloud has a larger optical thickness. After the maximum, the light curve of an optically thick cloud drops faster than with an optically thin cloud. The linear polarization degree decreases with increased optical thickness, and its preferential polarization direction is always perpendicular to the global scattering plane. A larger-sized dust cloud scatters more light to the observer so the light-curve magnitude increases monotonically with increased dust cloud size. The degree of linear polarization is not sensitive to the dust cloud size. The dust cloud shape mainly affects the LE light-curve shape around its global maximum. Around the maximum, a spherical dust cloud has a curved light curve, whereas a cube-shaped dust cloud has a flat light curve.

The time variation of LE images of optically thick and thin clouds is very different. Because the dust cloud is absorptive, if the incident light is scattered too many times, most of the light energy is absorbed and cannot be observed in the LE. Therefore, only light encountering a little attenuation in the dust cloud can be detected. For an optically thin cloud, the observer can see that the whole cloud is illuminated. For an optically thick cloud, only its optically thin edges are visible to the observer. An optically thick spherical cloud looks like a ring and an optically thick cube-shaped cloud only has its bottom edge visible. The LE image is also determined by the SN 1987A light curves. The maximum of the SN 1987A light curve results in a local bright region in the LE seen as a bright strip. The bright strip moves along with the LE paraboloid. As a core-collapse SN, SN 1987A has a strong and short UV-bright shock breakout just after the explosion, so its *U*-band light curve has an impulse-like feature before the maxima in other bands. Therefore, the *U*-band LE has an impulse-response-like feature, which distinguishes it from the other bands' LEs.

The linear polarization pattern of an LE is also strongly dependent on optical thickness. The LE linear polarization pattern of an optically thin cloud spatially does not vary a lot, and its preferential polarization direction is perpendicular to the scattering plane. In contrast, the LE linear polarization pattern of an optically thick cloud has a large spatial variation. For example, in a spherical dust cloud LE, the linear polarization degree decreases in the regions closer to the LE image center. Its preferential polarization direction is radial on the illuminated ring and is perpendicular to the local scattering plane. In an optically thin cloud, the observable light at a certain point of an LE is the average of light experiencing various propagation paths. The spatial variation of linear polarization is thus insignificant. The averaged *U* Stokes parameter is zero because of symmetry. In an optically thick cloud, the observable light only focuses on the edge region and experiences similar paths. Thus, its linear polarization pattern keeps the local feature and has significant spatial variation.

We estimate the dust cloud size and optical thickness using the OGLE-IV OTDS AT 2019xis *I*-band light-curve observation and MCRTM simulations. The Levenberg–Marquardt method is utilized to minimize the cost function, Equation (6). The simulated light curves assuming various dust cloud optical

properties and shapes all can roughly fit the observation well, even though the simulated light curves cannot capture some detailed light-curve features. We also calculate the mass of the dust cloud using the estimated size, optical thickness, and extinction coefficient. With an LMC gas-to-dust ratio of 300, the total mass of the cloud is about 7.8–9.3 $M_{\odot}$. We use one of the best-fit dust cloud optical thickness and size value to calculate the LE light curves in the Swift UVOT bands with the SN 1987A spectra. It is found that the photometry data of SN are not enough to accurately model LEs in UV bands, because interstellar dust optical properties vary significantly in UV wavelengths, so the UV spectra of SNe are necessary in modeling SN UV LEs.

This study was supported by the National Science Foundation (grant No. AST-1817099). J.D. and P.B. were partially supported by NASA Astrophysics Data Analysis grant NNX17AF43G. The computations were conducted at the Texas A&M University Supercomputing Facility. This research has made use of the SVO Filter Profile Service (http://svo2.cab.inta-csic.es/theory/fps/) supported from the Spanish MINECO through grant AYA2017-84089. We thank Nicholas Suntzeff for helpful discussions. We also thank Steven R. Schroeder for helping checking the grammar.

Facilities: HST(STIS), OGLE-IV OTDS.

Software: astropy (Astropy Collaboration et al. 2013).

Appendix A
HST Image Data Information

Table A1 lists information of the HST images used to generate Figure 2.

Table A1
Pre-echo Hubble Space Telescope Imaging

Dataset ID	Filter	Start Time (UTC)	Exposure Time (s)
ICD601BMQ	F475W	2014 Aug 16 11:13:44	600
ICD602DDQ	F475W	2014 Aug 16 15:59:09	600
ICD603GDQ	F475W	2014 Aug 17 06:15:23	600
ICD604I4Q	F475W	2014 Aug 17 11:00:48	600
ICD605LPQ	F475W	2014 Aug 20 04:06:25	600
ICD6010J0	F606W	2014 Aug 16 09:57:21	980
ICD6020J0	F606W	2014 Aug 16 14:43:48	980
ICD6030J0	F606W	2014 Aug 17 04:40:21	980
ICD6040J0	F606W	2014 Aug 17 09:50:03	980
ICD6050J0	F606W	2014 Aug 20 02:50:16	980
ICD6010L0	F814W	2014 Aug 16 10:24:53	1230
ICD6020L0	F814W	2014 Aug 16 15:11:20	1230
ICD6030L0	F814W	2014 Aug 17 05:07:53	1230
ICD6040L0	F814W	2014 Aug 17 10:17:35	1230
ICD6050L0	F814W	2014 Aug 20 03:32:44	1230

Appendix B
Monte Carlo Radiative Transfer Model

The MCRTM is based on a forward photon-tracing technique. Here a photon represents a very small portion of light power emitted by the source (e.g., SN 1987A). A random number determines the photon-scattering location, and its scattering direction is estimated according to the scattering phase function. The individual photon's total path length and Stokes vector are monitored.

The position of a photon is expressed in Cartesian coordinates as

$$\boldsymbol{r} = r\left(\sin\theta_r\cos\phi_r,\ \ \sin\theta_r\sin\phi_r,\ \ \cos\theta_r\right), \tag{B1}$$

where θ_r and ϕ_r are the zenith and azimuth angles of the position vector in laboratory coordinates, respectively, and r is the distance between the photon and coordinate origin. Laboratory coordinates refer to a fixed xyz Cartesian coordinate system. Here, the origin O is at the light source, the z-axis is along the line of sight to the observer, and the xy axes are perpendicular to z at the light source. Coordinates of all photon propagation and scattering events are expressed in this fixed system without transforming axes as each photon changes direction. The photons propagation direction is expressed as

$$\hat{e} = \left(\sin\theta_e\cos\phi_e,\ \ \sin\theta_e\sin\phi_e,\ \ \cos\theta_e\right), \tag{B2}$$

where θ_e and ϕ_e are the zenith and azimuth angles of the directional vector in laboratory coordinates.

In the MCRTM, a scattering event occurs at the photon's position $\boldsymbol{r}$. From the current scattering position $\boldsymbol{r}_s$ to the next scattering position $\boldsymbol{r}_{s+1}$, the path length is d_s and satisfies

$$d_s\hat{e}_s = \boldsymbol{r}_{s+1} - \boldsymbol{r}_s, \tag{B3}$$

where the subscript s denotes the scattering order. The path length is obtained as

$$\tau_s = \int_0^{d_s} C_{\rm ext}^s(r')dr' = -\ln\left[1 - \xi_1(1 - e^{-\tau_t})\right], \tag{B4}$$

where τ_s is the optical thickness from $\boldsymbol{r}_s$ to $\boldsymbol{r}_{s+1}$, $C_{\rm ext}^s$ is the extinction coefficient along the path from $\boldsymbol{r}_s$ to $\boldsymbol{r}_{s+1}$, τ_t is the optical thickness along $\hat{e}_s$ from $\boldsymbol{r}_s$ to the boundary of the scattering medium, and ξ_1 is a random number between 0 and 1. Equation (B4) guarantees $\boldsymbol{r}_{s+1}$ is always in the scattering medium and imposes a weight $w_s = 1 - e^{-\tau_t}$ on this photon's contribution.

At $\boldsymbol{r}_{s+1}$, the new propagation direction of the photon is determined by $\hat{e}_s$, scattering angle Θ_{s+1}, and azimuth angle Φ_{s+1}. Θ_{s+1} and Φ_{s+1} are angles in a local coordinate, where $\hat{e}_s$ is in the local z-direction along the preceding propagation

direction. Θ_{s+1} and Φ_{s+1} are computed as

$$\frac{\int_0^{\Theta_{s+1}} F_{11}(\boldsymbol{r}_{s+1}, \Theta')\sin\Theta' \, d\Theta'}{\int_0^{\pi} F_{11}(\boldsymbol{r}_{s+1}, \Theta')\sin\Theta' \, d\Theta'} = \xi_2, \tag{B5}$$

$$\Phi_{s+1} = 2\pi\xi_3, \tag{B6}$$

where F_{11} is the scattering phase function or the (1, 1) element of the scattering phase matrix, and ξ_2 and ξ_3 are two independent random numbers with a probability of a uniform distribution between 0 and 1. The zenith and azimuth angles of $\hat{e}_{s+1}$ in laboratory coordinates are

$$\theta_e^{s+1} = \arccos(\cos\Theta_{s+1}\cos\theta_e^s + \sin\Theta_{s+1}\sin\theta_e^s\cos\Phi_{s+1}) \tag{B7}$$

and

$$\phi_e^s = \Theta_{s+1} + \arccos\left(\frac{\cos\Theta_{s+1} - \cos\theta_e^{s+1}\cos\theta_e^s}{\sin\theta_e^{s+1}\sin\theta_e^s}\right). \tag{B8}$$

The photon's Stokes vector at $\boldsymbol{r}_{s+1}$ is updated as

$$\begin{pmatrix} I \\ Q \\ U \\ V \end{pmatrix}_{s+1} = w_s\varpi(\boldsymbol{r}_{s+1})\boldsymbol{L}(\pi - \sigma_2)\boldsymbol{F}(\boldsymbol{r}_{s+1}, \Theta_{s+1})\boldsymbol{L}(-\sigma_1) \begin{pmatrix} I \\ Q \\ U \\ V \end{pmatrix}_s, \tag{B9}$$

where I, Q, U, and V are Stokes vector elements, $\boldsymbol{F}$ is the scattering phase matrix, ϖ is the SSA, and $\boldsymbol{L}$ is the rotation matrix in the form

$$\begin{pmatrix} 1 & 0 & 0 & 0 \\ 0 & \cos 2\sigma & \sin 2\sigma & 0 \\ 0 & -\sin 2\sigma & \cos 2\sigma & 0 \\ 0 & 0 & 0 & 1 \end{pmatrix}. \tag{B10}$$

$\boldsymbol{L}(-\sigma_1)$ rotates the polarization reference plane from the incident meridional plane (formed by $\hat{e}_s$ and laboratory z-direction) to the scattering plane (formed by $\hat{e}_s$ and $\hat{e}_{s+1}$). $\boldsymbol{L}(\pi - \sigma_2)$ rotates the polarization reference plane from the scattering plane to the scattering meridional plane (formed by $\hat{e}_{s+1}$ and laboratory z-direction). The angles σ_1 and σ_2 are thus derived as

$$\sigma_1 = \arccos\left(\frac{\cos\theta_e^{s+1} - \cos\Theta_{s+1}\cos\theta_e^s}{\sin\Theta_{s+1}\sin\theta_e^s}\right), \tag{B11a}$$

$$\sigma_2 = \arccos\left(\frac{\cos\theta_e^{s} - \cos\Theta_{s+1}\cos\theta_e^{s+1}}{\sin\Theta_{s+1}\sin\theta_e^{s+1}}\right). \tag{B11b}$$

In the traditional forward photon-tracing technique, only the photons exiting the scattering medium and propagating to the observational directions are counted as contributions to the simulated observed signal. Traditional forward photon tracing is inefficient because it usually needs more than 10 million photons to achieve a convergent result and sometimes still contains noticeable random noise. To improve efficiency (reducing the required photons to about 1/10), in this MCRTM, at every scattering event, we consider the contribution of a photon to the simulated observation signal.

At any scattering position $\boldsymbol{r}_{s+1}$, the photons' contribution to the simulated observation signal Stokes vector is computed as

$$\begin{pmatrix} I \\ Q \\ U \\ V \end{pmatrix}_o = \frac{w_s}{4\pi}\exp(-\tau'_t)\varpi(\boldsymbol{r}_{s+1})\boldsymbol{L}(\pi - \sigma'_2)\boldsymbol{F}(\boldsymbol{r}_{s+1}, \Theta_o)\boldsymbol{L}(-\sigma'_1) \times \begin{pmatrix} I \\ Q \\ U \\ V \end{pmatrix}_s, \tag{B12'}$$

where the subscript o denotes observation, the scattering angle Θ_o is between $\hat{e}_s$ and the observer direction $\hat{e}_o$ (i.e., $\cos\Theta_o = \hat{e}_s \cdot \hat{e}_o$), σ'_1 and σ'_2 are determined in the same way as in Equation (B11), and τ'_t is the optical thickness from the scattering location to the observer. In one scattering event, we can specify different observer directions and obtain the photons' contribution to multiple directions. With the same number of simulated photons, the Monte Carlo photon tracing converges much faster than the traditional approach, if Equation (B12) is used to count photon contributions.

At a scattering position $\boldsymbol{r}_s$, the photons' total path length is

$$d_s^{\text{tot}} = \sum_{i=1}^{s} d_i. \tag{B13}$$

The delay time relative to the time when the source light directly propagates to the observer is derived according to a geometric relation (Patat 2005):

$$t_s^d = \frac{d_{\text{tot}} - \hat{e}_o \cdot \boldsymbol{r}_s - l_{\text{SN}}}{c}, \tag{B14}$$

where c is the speed of light, and l_{SN} is the distance between the observer and source. In the MCRTM, delay time bins are predefined with spacing Δt. If t_s^d is within a predefined time bin, the photons' contribution is counted toward the LE at the center of this time bin.

The observed Stokes vector computed by Equation (B12) must be normalized by the total emitted flux within the solid angle of the dust cloud viewed from SN 1987A. The normalization factor F_0 is defined as

$$F_0 = \frac{n_{\text{ph}}F_{\text{SN}}}{\Delta\Omega_{\text{ds}}\Delta t}, \tag{B15}$$

where n_{ph} is the total number of emitted photons, F_{SN} is the flux of the SN, and $\Delta\Omega_{\text{ds}}$ is the solid angle of the dust cloud viewing from the SN. Because the scattered flux is assumed to be linearly proportional to the source flux, by setting F_{SN} to be 1, we can directly multiply the radiative transfer result by the incident flux to obtain the scattered flux for a specific source. In the model, the SN is taken to be a point light source. If the dust cloud is a sphere, $\Delta\Omega_{\text{ds}}$ is computed as

$$\Delta\Omega_{\text{ds}} = 2\pi\left(1 - \frac{\sqrt{l_{\text{ds}}^2 - R_{\text{d}}^2}}{l_{\text{ds}}}\right), \tag{B16}$$

where R_d is the dust cloud sphere radius. To guarantee that all emitted photons propagate to the dust cloud, the photons' initial propagation direction is confined within $\Delta\Omega_{ds}$.

ORCID iDs

Jiachen Ding https://orcid.org/0000-0003-4928-6698
Peter Brown https://orcid.org/0000-0001-6272-5507

References

Arnett, W. D., Bahcall, J. N., Kirshner, R. P., & Woosley, S. E. 1989, ARA&A, 27, 629
Astropy Collaboration, Robitaille, T. P., Tollerud, E. J., et al. 2013, A&A, 558, A33
Bond, H. E., Gilmozzi, R., Meakes, M. G., & Panagia, N. 1990, ApJL, 354, L49
Breeveld, A. A., Landsman, W., Holland, S. T., et al. 2011, in AIP Conf. Ser. 1358, Gamma Ray Bursts 2010, ed. J. E. McEnery, J. L. Racusin, & N. Gehrels (Melville, NY: AIP), 373
Cardelli, J. A., Clayton, G. C., & Mathis, J. S. 1988, ApJL, 329, L33
Catchpole, R. M., Menzies, J. W., Monk, A. S., et al. 1987, MNRAS, 229, 15P
Catchpole, R. M., Whitelock, P. A., Feast, M. W., et al. 1988, MNRAS, 231, 75P
Catchpole, R. M., Whitelock, P. A., Menzies, J. W., et al. 1989, MNRAS, 237, 55P
Chevalier, R. A. 1986, ApJ, 308, 225
Chevalier, R. A., & Emmering, R. T. 1988, ApJL, 331, L105
Clayton, G. C., & Martin, P. G. 1985, ApJ, 288, 558
Couch, W. J., Allen, D. A., & Malin, D. F. 1990, MNRAS, 242, 555
Couderc, P. 1939, AnAp, 2, 271
Crotts, A. P. S. 1988, ApJL, 333, L51
Crotts, A. P. S. 2015, ApJL, 804, L37
Crotts, A. P. S., Kunkel, W. E., & McCarthy, P. J. 1989, ApJL, 347, L61
Draine, B. 2003a, ARA&A, 41, 241
Draine, B. T. 2003b, ApJ, 598, 1017
Draine, B. T., & Li, A. 2007, ApJ, 657, 810
Drozdov, D., Leising, M. D., Milne, P. A., et al. 2015, ApJ, 805, 71
Dwek, E., & Arendt, R. G. 2008, ApJ, 685, 976
Fitzpatrick, E. L. 1986, AJ, 92, 1068
Gehrels, N., Chincarini, G., Giommi, P., et al. 2004, ApJ, 611, 1005
Gouiffes, C., Rosa, M., Melnick, J., et al. 1988, A&A, 198, L9
Guillochon, J., Parrent, J., Kelley, L. Z., & Margutti, R. 2017, ApJ, 835, 64
Henyey, L. C., & Greenstein, J. L. 1941, ApJ, 93, 70
Kozłowski, S., Udalski, A., Wyrzykowski, L., et al. 2013, AcA, 63, 53
Landolt, A. U. 2009, AJ, 137, 4186
Li, A., & Draine, B. T. 2001, ApJ, 554, 778
McCray, R., & Fransson, C. 2016, ARA&A, 54, 19
Menzies, J. W., Catchpole, R. M., van Vuuren, G., et al. 1987, MNRAS, 227, 39P
Patat, F. 2005, MNRAS, 357, 1161
Patat, F., Benetti, S., Cappellaro, E., & Turatto, M. 2006, MNRAS, 369, 1949
Perlmutter, S., Aldering, G., Valle, M. D., et al. 1998, Natur, 391, 51
Phillips, M. M., Hamuy, M., Heathcote, S. R., Suntzeff, N. B., & Kirhakos, S. 1990, AJ, 99, 1133
Phillips, M. M., Heathcote, S. R., Hamuy, M., & Navarrete, M. 1988, AJ, 95, 1087
Pun, C. S. J., Kirshner, R. P., Sonneborn, G., et al. 1995, ApJS, 99, 223
Rest, A., Matheson, T., Blondin, S., et al. 2008, ApJ, 680, 1137
Rest, A., Prieto, J. L., Walborn, N. R., et al. 2012a, Natur, 482, 375
Rest, A., Sinnott, B., & Welch, D. L. 2012b, PASA, 29, 466
Rest, A., Suntzeff, N. B., Olsen, K., et al. 2005, Natur, 438, 1132
Riess, A. G., Press, W. H., & Kirshner, R. P. 1996, ApJ, 473, 88
Rodgers, C. D. 2000, Inverse Methods for Atmospheric Sounding: Theory and Practice (Singapore: World Scientific)
Rodrigo, C., & Solano, E. 2020, in The SVO Filter Service, the XIV.0 Scientific Meeting of the Spanish Astronomical Society *(Virtual, 13-15 July 2020)*, 182
Rodrigo, C., Solano, E., & Bayo, A. 2012, SVO Filter Profile Service Version 1.0 , IVOA Working Draft 2012 October 15
Roman-Duval, J., Gordon, K. D., Meixner, M., et al. 2014, ApJ, 797, 86
Roming, P. W. A., Kennedy, T. E., Mason, K. O., et al. 2005, SSRv, 120, 95
Schaefer, B. E. 1987, ApJL, 323, L47
Sparks, W. B. 1994, ApJ, 433, 19
Sugerman, B. E. K. 2003, AJ, 126, 1939
Sugerman, B. E. K., Crotts, A. P. S., Kunkel, W. E., Heathcote, S. R., & Lawrence, S. S. 2005a, ApJS, 159, 60
Sugerman, B. E. K., Crotts, A. P. S., Kunkel, W. E., Heathcote, S. R., & Lawrence, S. S. 2005b, ApJ, 627, 888
Suntzeff, N. B., Heathcote, S., Weller, W. G., et al. 1988, Natur, 334, 135
Taubenberger, S., Malesani, D., Terreran, G., et al. 2019, Transient Name Server AstroNote, 2019–163
Tylenda, R. 2004, A&A, 414, 223
Udalski, A., Szymański, M. K., & Szymański, G. 2015, AcA, 65, 1
Wampler, E. J., Wang, L., Baade, D., et al. 1990, ApJL, 362, L13
Wang, L. 2005, ApJL, 635, L33
Wang, L., Dyson, J. E., & Kahn, F. D. 1993, MNRAS, 261, 391
Wang, L., & Mazzali, P. A. 1992, Natur, 355, 58
Wang, L., & Wampler, E. J. 1992, A&A, 262, L9
Wang, L., & Wheeler, J. C. 1996, ApJL, 462, L27
Wang, X., Li, W., Filippenko, A. V., et al. 2008, ApJ, 677, 1060
Weingartner, J. C., & Draine, B. T. 2001, ApJ, 548, 296
Whitelock, P. A., Catchpole, R. M., Menzies, J. W., et al. 1988, MNRAS, 234, 5P
Witt, A. N. 1977, ApJS, 35, 1
Wyrzykowski, L., Kostrzewa-Rutkowska, Z., Kozlowski, S., et al. 2014, AcA, 64, 197
Xu, J., Crotts, A. P. S., & Kunkel, W. E. 1995, ApJ, 451, 806
Yang, Y., Wang, L., Baade, D., et al. 2017, ApJ, 834, 60
Yaron, O., & Gal-Yam, A. 2012, PASP, 124, 668